ELSEVIER

Comput. Methods Appl. Mech. Engrg. 151 (1998) 377–400

Computer methods in applied mechanics and engineering

A Voronoi cell finite element model for particle cracking in elastic–plastic composite materials

Suresh Moorthy, Somnath Ghosh*

Department of Aerospace Engineering, Applied Mechanics and Aviation, The Ohio State University, Columbus, OH 43210, USA

Received 7 January 1997

Abstract

In this paper, a small deformation Voronoi Cell finite element model is developed for damage in particle reinforced composite materials by particle cracking and splitting. It incorporates a ductile elastic–plastic matrix material containing any dispersion of brittle elastic inclusions of arbitrary shapes and sizes. Damage initiation by micro-cracking or splitting of the inclusions is assumed to follow a maximum principal stress theory or Rankine criterion. Complete particle cracking or splitting is assumed at the onset of damage. The model accounts for microstructure evolution through progressive particle fracture in complex morphologies without any user interference. Various microstructural morphologies are simulated to verify the effectiveness of the model. Analysis of real microstructures from optical micrographs of Al–Si–Mg composite systems, is conducted to demonstrate the promise of this numerical model.

1. Introduction

Despite mechanical property enhancements, the presence of second phase inclusions in many composite systems has adverse effects on failure properties like ductility and fracture toughness. The degree of this influence depends on microstructural morphology like size, shape, orientation and spatial distribution of heterogeneities, and on constituent material properties. Voids may nucleate by particle splitting or interface decohesion, grow with large plastic deformation, and finally coalesce to cause overall structural failure. Clustered microstructures are particularly vulnerable to premature fracture by this mechanism. Rigorous fundamental studies are warranted for understanding deformation and failure mechanisms, prior to design of composite materials in high performance applications. Studies reflecting the details of actual heterogeneous microstructures are very important. It is through these studies, that the actual evolution of state and material variables in materials can be predicted.

Within the framework of continuum damage mechanics, two distinct approaches, namely the phenomenological and micromechanical approaches have evolved. Motivated by experimental observations, the phenomenological theories [1] introduce a set of scalar or tensor damage evolution parameters as internal variables in the constitutive requirements of irreversible thermodynamics processes, with their growth determined by appropriate evolution laws. The empirical treatment of morphological effects such as spatial distribution, size effects makes the application of these models to many materials questionable [2,3]. Micromechanical theories, on the other hand, employ continuum mechanics principles at the microscopic level to predict overall constitutive response [4,5]. While some of these models [4] provide reasonable predictions of overall properties for a dilute distribution of damage entities, others [5] attempt to analyze the interaction effects between damage

---

* Corresponding author.

0045-7825/98/$19.00 © 1998 Elsevier Science S.A. All rights reserved

PII S0045-7825(97)00160-6

entities introduced by the morphological characteristics of the microstructure. Recently, novel approaches to integrate micromechanical and computational approaches at the microscale with phenomenological approaches in the macroscale have also been proposed [2,6]. While many of these methods can model damage in brittle homogeneous materials, far fewer analytical models are available for ductile, two phase composition of the microstructure. Small scale yielding solutions using asymptotic analysis for a single bi-material interface due to Shih and Asaro [7] and Hutchinson et al. [8] are notable exceptions.

Evolving damage in heterogeneous media with a mixture of ductile and brittle constituents have been numerically modeled using *Unit Cell* methods. These methods assume that the material is constituted of periodic repetition of unit cells, identified as representative volume elements (RVE) of the microstructure. Displacement based finite element analysis is used to analyze the RVE in order to predict the onset and growth of evolving damage. Notable among these are the finite element simulations by Tvergaard [9], Bao [10], Hom [11], Suresh et al. [12] and Needleman et al. [13]. In [9–12], simple microstructures with pre-existing damaged heterogeneities are considered. In [13] a finite element mesh which allows for crack growth by element separation is used to simulate the microscale unit cell. While these models provide valuable insights into the microstructural damage processes, the simple morphologies considered grossly idealize actual microstructures for many engineering materials. Micrographs of real heterogeneous materials often exhibit randomness in shape, size and location. To circumvent these deficiencies, Suresh and coworkers [14,15], McHugh et al. [16] among others, have made novel progresses in computational modeling of discontinuously reinforced materials with random spatial dispersion. However, a very high resolution of finite element mesh is required even for undamaged heterogeneous media, and enormous computational efforts are required to capture failure by these models.

Recent experimental studies on actual heterogeneous materials indicate that microstructural morphology can play a vital role in the structural failure of mutiphase materials. Scanning electron microscopy of damaged microstructures by Hunt et al. [17,18] and Kiser and Zok [19] show particle distribution, size and shape can significantly alter the extent of microstructural damage and the onset of material failure. Complete microstructural damage, as assumed by many computational models through the periodicity constraint, is usually a rarity in most microstructures [18,19]. Preferential damage is usually a function of matrix straining and particle locations.

The Voronoi cell finite element model (VCFEM), developed by Ghosh and coworkers [20–22], has shown significant promise as an effective tool for small deformation elastic-plastic analysis of random heterogeneous materials. The key idea behind VCFEM formulation is to combine the fundamental concepts of finite element methods with essential characteristics of micromechanics approaches, to yield a powerful material based element. In this method, the finite element mesh evolves naturally by Dirichlet Tessellation of a representative material microstructure to discretize the domain into a network of multi-sided convex 'Voronoi' polygons or cells. Each Voronoi cell containing one second phase inclusion at most, as shown in Fig. 1, is used as a finite element without any further discretization. In this paper, a VCFEM is developed for analysis of damage evolution in particulate reinforced composite materials with arbitrary dispersions. Damage in the microstructure is introduced through cracking and splitting of particles. Damage initiation is assumed to follow a maximum principal stress theory or Rankine criterion. Complete particle cracking or splitting is assumed at the onset of damage. The computational model is capable of accounting for damage initiation and propagation in

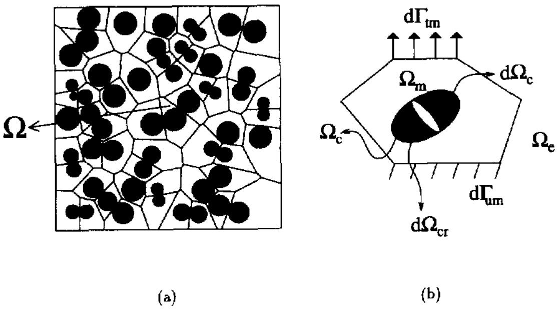

(a) (b)

Fig. 1. (a) Representative material element; (b) Voronoi cell finite element with cracked particle.

microstructural models of real micrographs without any idealizations. The finite element model is validated through comparisons with various analytical models, other studies in literature and simulations with conventional finite element packages. The effectiveness of VCFEM in modelling particle cracking for real composite micrographs is tested, and its potential in predicting material failure is discussed.

2. Particle cracking with the Voronoi cell finite element method (VCFEM)

Damage initiation at different sites of the microstructure is modeled in the form of particle cracking or splitting, that is triggered by a maximum principal stress criterion, also known as the Rankine criterion. In particle cracking, the crack is completely contained within the inclusion, while in the case of particle splitting, the crack tip extends nominally into the matrix. A major assumption that is made is that complete particle cracking and splitting occurs at the onset of damage, thereby avoiding the problem of crack propagation within each inclusion. In the context of the problems considered, this assumption is justified from two points of view, viz. (a) for the multitude of inclusions considered, crack propagation in each inclusion would make the problem inordinately large and (b) experimental observations indicate very rapid transition from initiation of particle cracking to complete splitting. In the Voronoi cell finite element model, this implies that the topology of each element changes from two constituent phases (for undamaged inclusions) to three constituents (for inclusions with a crack) as shown in Fig. 1. The crack phase in the damaged element is represented by an elliptical void with a high aspect ratio (~10–100).

2.1. *Assumed stress hybrid formulation for Voronoi cell elements with damage*

The assumed stress hybrid formulation that has been used in the VCFEM development for undamaged heterogeneous materials in [20–22] is extended in this paper to accommodate the crack phase. Consider a typical representative material element consisting of N damaged or undamaged particles that are contained in each of the N Voronoi cell elements, as shown in Fig. 1. Each Voronoi cell serves as a *basic structural element* (BSE) of the microstructure, that represents the region of a heterogeneity with its matrix neighborhood. The matrix, inclusion and crack phase in each Voronoi cell are denoted by Ω_m, Ω_c and Ω_{cr}, respectively, while each element boundary $\partial\Omega_e$ is assumed to be comprised of a prescribed traction boundary Γ_{tm}, a prescribed displacement boundary Γ_{um}, and an interelement boundary Γ_m, i.e. $\partial\Omega_e = \Gamma_{tm} \cup \Gamma_{um} \cup \Gamma_m$. The matrix-inclusion interface $\partial\Omega_c$ has an outward normal $\boldsymbol{n}^c$, the inclusion-crack interface $\partial\Omega_{\mathrm{cr}}$ has an outward normal $\boldsymbol{n}^{cr}$, and $\boldsymbol{n}^e$ is the outward normal to $\partial\Omega_e$.

The assumed stress hybrid formulation in the Voronoi cell finite element method (VCFEM) requires independent assumptions of an equilibriated stress field in the interior of each element Ω_e, and compatible displacement fields on the boundary $\partial\Omega_e$, and interfaces $\partial\Omega_c$ and $\partial\Omega_{\mathrm{cr}}$. In an incremental formulation for rate independent plasticity, let $\boldsymbol{\sigma}$ be an equilibriated stress field and $\boldsymbol{\epsilon}(\boldsymbol{\sigma}, \textit{loading path})$ be the associated strain field in Ω_e at the beginning of an increment. Let $\boldsymbol{u}$, $\boldsymbol{u}'$ and $\boldsymbol{u}''$ denote compatible displacement fields on $\partial\Omega_e$, $\partial\Omega_c$ and $\partial\Omega_{\mathrm{cr}}$, respectively. The incremental two field assumed stress hybrid variational formulation invokes an element energy functional of the form:

$$\begin{aligned}
\Pi_e^C(\Delta\boldsymbol{\sigma}, \Delta\boldsymbol{u}) = &-\int_{\Omega_e} \Delta B(\boldsymbol{\sigma}, \Delta\boldsymbol{\sigma})\,\mathrm{d}\Omega - \int_{\Omega_e} \boldsymbol{\epsilon} : \Delta\boldsymbol{\sigma}\,\mathrm{d}\Omega \\
&\int_{\partial\Omega_e} (\boldsymbol{\sigma} + \Delta\boldsymbol{\sigma}) \cdot \boldsymbol{n}^e \cdot (\boldsymbol{u} + \Delta\boldsymbol{u})\,\partial\Omega - \int_{\Gamma_{tm}} (\bar{t} + \Delta\bar{t}) \cdot (\boldsymbol{u} + \Delta\boldsymbol{u})\,\mathrm{d}\Gamma \\
&- \int_{\partial\Omega_c} (\boldsymbol{\sigma}^m + \Delta\boldsymbol{\sigma}^m - \boldsymbol{\sigma}^c - \Delta\boldsymbol{\sigma}^c) \cdot \boldsymbol{n}^c \cdot (\boldsymbol{u}' + \Delta\boldsymbol{u}')\,\partial\Omega - \int_{\partial\Omega_{\mathrm{cr}}} (\boldsymbol{\sigma}^c + \Delta\boldsymbol{\sigma}^c) \cdot \boldsymbol{n}^{\mathrm{cr}} \cdot (\boldsymbol{u}'' + \Delta\boldsymbol{u}'')\,\partial\Omega
\end{aligned} \tag{1}$$

where $\Delta\boldsymbol{B}$ is the increment of complimentary energy density in an element and, the superscripts m, c and cr correspond to variables associated with the matrix, inclusion and crack phases in each Voronoi cell element. The total energy for the entire heterogeneous domain is obtained by adding the element energy functionals

$$\Pi^C = \sum_{e=1}^{N} \Pi_e^C \tag{2}$$

Setting the first variation of Π_e^C with respect to stress increments $\Delta\boldsymbol{\sigma}$ to zero, results in the kinematic condition as the Euler equation,

$$\nabla \Delta \boldsymbol{u} = \Delta \boldsymbol{\epsilon} \quad \text{in } \Omega_e \tag{3}$$

and setting the first variation of Π^C with respect to the independent boundary displacements $\Delta\boldsymbol{u}$, $\Delta\boldsymbol{u}'$ and $\Delta\boldsymbol{u}''$ to zero, respectively, yield the following traction conditions as Euler equations,

$$(\boldsymbol{\sigma} + \Delta\boldsymbol{\sigma}) \cdot \boldsymbol{n}^{e+} = -(\boldsymbol{\sigma} + \Delta\boldsymbol{\sigma}) \cdot \boldsymbol{n}^{e-} \quad \text{on } \Gamma_m \quad \textit{Interelement traction reciprocity} \tag{4}$$

$$(\boldsymbol{\sigma} + \Delta\boldsymbol{\sigma}) \cdot \boldsymbol{n}^{e} = \bar{t} + \overline{\Delta t} \quad \text{on } \Gamma_{tm} \quad \textit{Traction boundary conditions} \tag{5}$$

$$(\boldsymbol{\sigma}^c + \Delta\boldsymbol{\sigma}^c) \cdot \boldsymbol{n}^{c} = (\boldsymbol{\sigma}^m + \Delta\boldsymbol{\sigma}^m) \cdot \boldsymbol{n}^{c} \quad \text{on } \partial\Omega_c \quad \textit{Interface traction reciprocity} \tag{6}$$

$$(\boldsymbol{\sigma}^c + \Delta\boldsymbol{\sigma}^c) \cdot \boldsymbol{n}^{\mathrm{cr}} = 0 \quad \text{on } \partial\Omega_{\mathrm{cr}} \quad \textit{Zero traction on crack boundary} \tag{7}$$

Superscript + and − denote elements on both sides of the boundary Γ_m. The assumed equilibriated stress fields $\Delta\boldsymbol{\sigma}$ and compatible displacement fields $\Delta\boldsymbol{u}$, $\Delta\boldsymbol{u}'$ and $\Delta\boldsymbol{u}''$, the stress–strain relationships ($\partial\, \Delta B / \partial\, \Delta\boldsymbol{\sigma} = \Delta\boldsymbol{\epsilon}$), along with the Euler equations (3)–(7) completely define the incremental problem for a heterogeneous material.

2.2. Element formulations and assumptions

2.2.1. Stress functions for Voronoi elements without damage

Independent assumptions on stress increments $\Delta\boldsymbol{\sigma}$ are made in the matrix and inclusion phases to accommodate stress jumps across the interface. In two-dimensional analysis, the Airy's stress function $\boldsymbol{\Phi}(x, y)$ is a convenient tool for deriving equilibriated stress-increments, in which components of $\Delta\boldsymbol{\sigma}$ are expressed as

$$\Delta\sigma_{xx} = \frac{\partial^2 \boldsymbol{\Phi}}{\partial y^2}, \qquad \Delta\sigma_{yy} = \frac{\partial^2 \boldsymbol{\Phi}}{\partial x^2}, \qquad \Delta\sigma_{xy} = -\frac{\partial^2 \boldsymbol{\Phi}}{\partial x\, \partial y} \tag{8}$$

In an attempt to incorporate essential aspects of micromechanics in the choice of stress functions, Moorthy and Ghosh [20] have introduced a decomposition of the matrix stress functions into (a) a purely polynomial function $\boldsymbol{\Phi}^m_{\mathrm{poly}}$ and (b) a *reciprocal* function $\boldsymbol{\Phi}^m_{\mathrm{rec}}$, for two phase composites. Thus, the stress field in the matrix-phase of Voronoi cell elements are derived from the Airy's stress function $\boldsymbol{\Phi}^m = \boldsymbol{\Phi}^m_{\mathrm{poly}} + \boldsymbol{\Phi}^m_{\mathrm{rec}}$, while that in the inclusion-phase is obtained from a purely polynomial representation $\boldsymbol{\Phi}^c = \boldsymbol{\Phi}^c_{\mathrm{poly}}$. The reciprocal function $\boldsymbol{\Phi}^m_{\mathrm{rec}}$ facilitates stress concentration accounting for the shape of the inclusion, satisfies traction reciprocity at the interface $\partial\Omega_c$, as well as decays at large distances from the interface. The pure polynomial function $\boldsymbol{\Phi}^m_{\mathrm{poly}}$ on the other hand, accommodates the traction field on the element boundary $\partial\Omega_e$. The polynomial terms in the matrix/inclusion is written as

$$\boldsymbol{\Phi}^{m/c}_{\mathrm{poly}} = \sum_{p,q} \xi^p \eta^q \, \Delta\beta^{m/c}_{pq} \tag{9}$$

where (ξ, η) correspond to scaled local coordinates with origin at the element centroid (x_c, y_c), written as

$$\xi = (x - x_c)/L \tag{10}$$

$$\eta = (y - y_c)/L \tag{11}$$

and the scale parameter $L = \sqrt{\max(x - x_c)\max(y - y_c)}\ \forall\ (x, y) \in \partial\Omega_e$. The use of the local coordinates (ξ, η) instead of global coordinates (x, y), prevents numerical inaccuracies due to high exponents of (x, y) in $\boldsymbol{\Phi}^{m/c}$, and thus avoid ill-conditioning of the element stiffness matrices.

As mentioned earlier, the effect of shape on state variables should be dominant near the interface and vanish in the far-field. Additionally, the traction field in the matrix should provide for matching the inclusion traction field at the interface for composite materials, and reduce to zero for porous materials. These features are introduced through the reciprocal function $\boldsymbol{\Phi}^m_{\mathrm{rec}}$ which can account for stress concentrations arising from the presence of the heterogeneity. In the construction of $\boldsymbol{\Phi}^m_{\mathrm{rec}}$, a transformed *radial* coordinate f is first generated by either a Schwarz–Christoffel conformal transformation [23,24] (for elliptical heterogeneities) or by a Fourier series transformation [20] of the interface $\partial\Omega_c$ (for arbitrary shaped heterogeneities, e.g. squares). The transformed radial coordinate f satisfies the conditions $f \to \infty$ as $(x, y) \to \infty$, and $f = 1$ on the interface $\partial\Omega_c$. $\boldsymbol{\Phi}^m_{\text{rec}}$ is then expressed as

$$\boldsymbol{\Phi}^m_{\text{rec}} = \sum_{p,q} \xi^p \eta^q \sum_{i=1}^{n} \frac{1}{f^{p+q+i-1}} \Delta\beta^m_{pqi} \tag{12}$$

Increment of the stress vector $\Delta \boldsymbol{t}^m$ is related to $\boldsymbol{\Phi}^m$ from Eq. (8) as

$$\Delta t^m_x = \frac{\partial \boldsymbol{\Phi}^m}{\partial y}, \qquad \Delta t^m_y = -\frac{\partial \boldsymbol{\Phi}^m}{\partial x}$$

Substituting Eqs. (9) and (12) in the above expression, together with the relation $\partial/\partial(x_i) = L\, \partial/\partial(\xi_i)$, the traction increments are obtained as

$$\begin{aligned}
\Delta t^m_x &= \sum_{p,q} q \xi^p \eta^{q-1} \left(\Delta\beta^m_{pq} + \sum_{i=p+q}^{n} \Delta\beta^m_{pqi} \frac{1}{f^i} \right) - \sum_{p,q} \xi^p \eta^q \sum_{i=p+q}^{n} \Delta\beta^m_{pqi}\, i \frac{1}{f^{i+1}} \frac{\partial f}{\partial \eta} \\
\Delta t^m_y &= -\sum_{p,q} p \xi^{p-1} \eta^q \left(\Delta\beta^m_{pq} + \sum_{i=p+q}^{n} \Delta\beta^m_{pqi} \frac{1}{f^i} \right) + \sum_{p,q} \xi^p \eta^q \sum_{i=p+q}^{n} \Delta\beta^m_{pqi}\, i \frac{1}{f^{i+1}} \frac{\partial f}{\partial \xi}
\end{aligned} \tag{13}$$

Coefficients $\Delta\beta^m_{pqi}$ in first set of terms in Eq. (13) add flexibility to polynomial coefficients $\Delta\beta^m_{pq}$ in the stress expansions for matching desired tractions at the interface ($f = 1$). The gradient of f in second set of terms account for the shape of the interface. Terms produced by the reciprocal function in Eq. (13) have negligible effects on the traction vector far away from the heterogeneity due to f becoming extremely large. In other words, the far-field tractions are produced predominantly by polynomial terms in the stress function and are unaffected by shape of the heterogeneity. Stress increments in the matrix and undamaged inclusion phases of Voronoi cell elements are obtained from (8) as

$$\begin{aligned}
\begin{Bmatrix} \Delta\sigma^m_{xx} \\ \Delta\sigma^m_{yy} \\ \Delta\sigma^m_{xy} \end{Bmatrix} &= \begin{Bmatrix} \displaystyle\sum_{p,q} \frac{\partial^2(\xi^p\eta^q)}{\partial\eta^2} \Delta\beta^m_{pq} + \sum_{p,q,i} \frac{\partial^2(\xi^p\eta^q/f^i)}{\partial\xi^2} \Delta\beta^m_{pqi} \\ \displaystyle\sum_{p,q} \frac{\partial^2(\xi^p\eta^q)}{\partial\xi^2} \Delta\beta^m_{pq} + \sum_{p,q,i} \frac{\partial^2(\xi^p\eta^q/f^i)}{\partial\xi^2} \Delta\beta^m_{pqi} \\ \displaystyle -\sum_{p,q} \frac{\partial^2(\xi^p\eta^q)}{\partial\xi\,\partial\eta} \Delta\beta^m_{pq} - \sum_{p,q,i} \frac{\partial^2(\xi^p\eta^q/f^i)}{\partial\xi\,\partial\eta} \Delta\beta^m_{pqi} \end{Bmatrix} \\
&= [\boldsymbol{P}^m_{\text{poly}}] \begin{Bmatrix} \Delta\beta^m_{11} \\ \vdots \\ \Delta\beta^m_{pq} \\ \vdots \end{Bmatrix} + [\boldsymbol{P}^m_{\text{rec}}] \begin{Bmatrix} \Delta\beta^m_{111} \\ \vdots \\ \Delta\beta^m_{pqi} \\ \vdots \end{Bmatrix} \\
&= [\boldsymbol{P}^m]\{\Delta\boldsymbol{\beta}^m\}
\end{aligned} \tag{14}$$

and

$$\begin{aligned}
\begin{Bmatrix} \Delta\sigma^c_{xx} \\ \Delta\sigma^c_{yy} \\ \Delta\sigma^c_{xy} \end{Bmatrix} &= \begin{Bmatrix} \displaystyle\sum_{p,q} \frac{\partial^2(\xi^p\eta^q)}{\partial\eta^2} \Delta\beta^c_{pq} \\ \displaystyle\sum_{p,q} \frac{\partial^2(\xi^p\eta^q)}{\partial\xi^2} \Delta\beta^c_{pq} \\ \displaystyle -\sum_{p,q} \frac{\partial^2(\xi^p\eta^q)}{\partial\eta\,\partial\eta} \Delta\beta^c_{pq} \end{Bmatrix} \\
&= [\boldsymbol{P}^c]\{\Delta\boldsymbol{\beta}^c\}
\end{aligned} \tag{15}$$

2.2.2. *Stress functions for Voronoi cell elements with cracked particles*

At the onset of particle cracking, a third phase in the form of an elliptical void representing a blunt crack, is added to the Voronoi cell element. This transition in element topology from two to three phases, requires automatic adjustments in stress functions and associated stress fields in Eq. (12). In this process, the crack is assumed to be of elliptical shape with a high aspect ratio (~10–100). The crack boundary $\partial\Omega_{\mathrm{cr}}$ may be parametrically represented by an equation $f_{\mathrm{cr}}(x, y) = 1$, where $f_{\mathrm{cr}}(x, y)$ is obtained through conformal mapping of the ellipse. f_{cr} represents a specialized radial coordinate with the property, $f_{\mathrm{cr}} \to \infty$ as $(x, y) \to \infty$. Airy's functions for the matrix and inclusion phases are then constructed by superposing reciprocal terms derived from the conformal mapping function f_{cr} on the functions for undamaged elements.

$$\begin{aligned} \Phi^m &= \Phi^m_{\mathrm{poly}} + \Phi^m_{\mathrm{rec}} + \Phi^{mc}_{\mathrm{rec}} \\ \Phi^c &= \Phi^c_{\mathrm{poly}} + \Phi^{cc}_{\mathrm{rec}} \end{aligned} \tag{16}$$

where Φ^{mc}_{rec} and Φ^{cc}_{rec} are contributions due to the crack, written as

$$\begin{aligned} \Phi^{mc}_{\mathrm{rec}} &= \sum_{p,q} \xi^p \eta^q \sum_{i=1}^{n'} \left(\frac{\Delta\beta^{mc}_{pqi}}{f_{\mathrm{cr}}^{p+q+i-1}} \right) \\ \Phi^{cc}_{\mathrm{rec}} &= \sum_{p,q} \xi^p \eta^q \sum_{i=1}^{n'} \left(\frac{\Delta\beta^{cc}_{pqi}}{f_{\mathrm{cr}}^{p+q+i-1}} \right) \end{aligned} \tag{17}$$

While the reciprocal terms $(1/f_{cr}^{p+q+i-1})$ in Φ^{cc}_{rec} facilitate zero traction condition on the crack boundary $\partial\Omega_{\mathrm{cr}}$, their presence in Φ^{mc}_{rec} provides *asymptotic* stress gradients in the matrix material near the crack tip. Stress components resulting from these functions are

$$\begin{aligned} \begin{Bmatrix} \Delta\sigma^m_{xx} \\ \Delta\sigma^m_{yy} \\ \Delta\sigma^m_{xy} \end{Bmatrix} &= \begin{Bmatrix} \dfrac{\partial^2 \Phi^m_{\mathrm{poly}}}{\partial\eta^2} \Delta\beta^m_{pq} + \dfrac{\partial^2 \Phi^m_{\mathrm{rec}}}{\partial\eta^2} \Delta\beta^m_{pqi} + \dfrac{\partial^2 \Phi^{mc}_{\mathrm{rec}}}{\partial\eta^2} \Delta\beta^{mc}_{pqi} \\ \dfrac{\partial^2 \Phi^m_{\mathrm{poly}}}{\partial\xi^2} \Delta\beta^m_{pq} + \dfrac{\partial^2 \Phi^m_{\mathrm{rec}}}{\partial\xi^2} \Delta\beta^m_{pqi} + \dfrac{\partial^2 \Phi^{mc}_{\mathrm{rec}}}{\partial\xi^2} \Delta\beta^{mc}_{pqi} \\ -\dfrac{\partial^2 \Phi^m_{\mathrm{poly}}}{\partial\xi\,\partial\eta} \Delta\beta^m_{pq} - \dfrac{\partial^2 \Phi^m_{\mathrm{rec}}}{\partial\xi\,\partial\eta} \Delta\beta^m_{pqi} - \dfrac{\partial^2 \Phi^{mc}_{\mathrm{rec}}}{\partial\xi\,\partial\eta} \Delta\beta^{mc}_{pqi} \end{Bmatrix} \\ &= [\boldsymbol{P}^m]\{\Delta\boldsymbol{\beta}^m\} \\ \begin{Bmatrix} \Delta\sigma^c_{xx} \\ \Delta\sigma^c_{yy} \\ \Delta\sigma^c_{xy} \end{Bmatrix} &= \begin{Bmatrix} \dfrac{\partial^2 \Phi^c_{\mathrm{poly}}}{\partial\eta^2} \Delta\beta^c_{pq} + \dfrac{\partial^2 \Phi^{cc}_{\mathrm{rec}}}{\partial\eta^2} \Delta\beta^{cc}_{pqi} \\ \dfrac{\partial^2 \Phi^c_{\mathrm{poly}}}{\partial\xi^2} \Delta\beta^c_{pq} + \dfrac{\partial^2 \Phi^{cc}_{\mathrm{rec}}}{\partial\xi^2} \Delta\beta^{cc}_{pqi} \\ -\dfrac{\partial^2 \Phi^c_{\mathrm{poly}}}{\partial\xi\,\partial\eta} \Delta\beta^c_{pq} - \dfrac{\partial^2 \Phi^{cc}_{\mathrm{rec}}}{\partial\xi\,\partial\eta} \Delta\beta^{cc}_{pqi} \end{Bmatrix} \\ &= [\boldsymbol{P}^c]\{\Delta\boldsymbol{\beta}^c\} \end{aligned} \tag{18}$$

2.2.3. *Compatible displacement fields along element boundaries and interfaces*

Compatible displacement increments are generated by interpolation in terms of generalized displacements at nodal points on $\partial\Omega_e$, $\partial\Omega_c$ and $\partial\Omega_{\mathrm{cr}}$. Compatible displacement fields on the interface $\partial\Omega_c$ imply perfect bonding in the case of composite materials. In two-dimensional analysis, linearly interpolated displacement increments on the boundary segment between the ith and $(i+1)$th nodal points are expressed as

$$\{\Delta\boldsymbol{u}\} = \begin{Bmatrix} \Delta u_x \\ \Delta u_y \end{Bmatrix} = \begin{bmatrix} 1 - a/l_i & 0 & a/l_i & 0 \\ 0 & 1 - a/l_i & 0 & a/l_i \end{bmatrix} \begin{Bmatrix} \Delta q_{2i-1} \\ \Delta q_{2i} \\ \Delta q_{2i+1} \\ \Delta q_{2i+2} \end{Bmatrix} \tag{19}$$

where l_i is the length of the ith segment and a is the distance from the ith node. The displacement increments on the Voronoi cell element boundary, the matrix-inclusion interface and the crack boundary may be respectively interpolated as

$$\begin{aligned}\{\Delta \boldsymbol{u}\} &= [\boldsymbol{L}^e]\{\Delta \boldsymbol{q}\}\\ \{\Delta \boldsymbol{u}'\} &= [\boldsymbol{L}^c]\{\Delta \boldsymbol{q}'\}\\ \{\Delta \boldsymbol{u}''\} &= [\boldsymbol{L}^{\mathrm{cr}}]\{\Delta \boldsymbol{q}''\}\end{aligned} \tag{20}$$

where $\{\Delta \boldsymbol{q}\}$, $\{\Delta \boldsymbol{q}'\}$ and $\{\Delta \boldsymbol{q}''\}$ are the generalized displacement increment vectors. In general, $[\boldsymbol{L}^e]$, $[\boldsymbol{L}^c]$ and $[\boldsymbol{L}^{cr}]$ are taken to be linear interpolation matrices. While linear interpolation on the boundary is economic, it leads to discontinuous normals at the nodes, thus degrading the solution especially on the crack boundary. To circumvent this, points $(x_{\mathrm{cr}}, y_{\mathrm{cr}})$ on the crack boundary are interpolated using a quadratic interpolation from three points on the ellipse.

$$\begin{Bmatrix} x_{\mathrm{cr}} \\ y_{\mathrm{cr}} \end{Bmatrix} = \begin{bmatrix} 2\left(1-\frac{a}{l_i}\right)\left(\frac{1}{2}-\frac{a}{l_i}\right) & 0 \\ 0 & 2\left(1-\frac{a}{l_i}\right)\left(\frac{1}{2}-\frac{a}{l_i}\right) \\ \left(1-\frac{a}{l_i}\right)\frac{a}{l_i} & 0 \\ 0 & \left(1-\frac{a}{l_i}\right)\frac{a}{l_i} \\ 2\frac{a}{l_i}\left(\frac{a}{l_i}-\frac{1}{2}\right) & 0 \\ 0 & 2\frac{a}{l_i}\left(\frac{a}{l_i}-\frac{1}{2}\right) \end{bmatrix}^{\mathrm{T}} \begin{Bmatrix} x_i \\ y_i \\ x_{i+1/2} \\ y_{i+1/2} \\ x_{i+1} \\ y_{i+1} \end{Bmatrix}$$

where (x_i, y_i) and (x_{i+1}, y_{i+1}) are the coordinates of two adjacent nodes, l_i is the curvilinear distance between them, a is the curvilinear distance between $(x_{\mathrm{cr}}, y_{\mathrm{cr}})$ and node i and $(x_{i+1/2}, y_{i+1/2})$ are coordinates of the mid-side node (i.e. at $a = l_i/$).

3.2.4. *Weak form resulting from element assumptions*

Substituting element approximations for stresses (18) and displacements (20) in the energy functional (1), and setting first variations with respect to the stress coefficients $\Delta\boldsymbol{\beta}^m$ and $\Delta\boldsymbol{\beta}^c$, respectively, to zero, results in the weak forms of the kinematic relations (3) as

$$\begin{aligned}\int_{\Omega_m} [\boldsymbol{P}^m]^{\mathrm{T}}\{\boldsymbol{\epsilon} + \Delta\boldsymbol{\epsilon}\}\,\mathrm{d}\Omega &= \int_{\partial\Omega_e} [\boldsymbol{P}^m]^{\mathrm{T}}[\boldsymbol{n}^e][\boldsymbol{L}^e]\,\mathrm{d}\Omega\{\Delta\boldsymbol{q}\} - \int_{\partial\Omega_c} [\boldsymbol{P}^m]^{\mathrm{T}}[\boldsymbol{n}^c][\boldsymbol{L}^c]\,\mathrm{d}\Omega\{\Delta\boldsymbol{q}'\}\\ \int_{\Omega_c} [\boldsymbol{P}^c]^{\mathrm{T}}\{\boldsymbol{\epsilon} + \Delta\boldsymbol{\epsilon}\}\,\mathrm{d}\Omega &= \int_{\partial\Omega_e} [\boldsymbol{P}^c]^{\mathrm{T}}[\boldsymbol{n}^c][\boldsymbol{L}^c]\,\mathrm{d}\Omega - \int_{\partial\Omega_{\mathrm{cr}}} [\boldsymbol{P}^c]^{\mathrm{T}}[\boldsymbol{n}^{\mathrm{cr}}][\boldsymbol{L}^{\mathrm{cr}}]\,\mathrm{d}\Omega\{\Delta\boldsymbol{q}''\}\end{aligned} \tag{21}$$

Additionally, setting the first variation of the total energy functional in Eq. (2) with respect to $\Delta\boldsymbol{q}$, $\Delta\boldsymbol{q}'$ and $\Delta\boldsymbol{q}''$, results in the weak form of the traction reciprocity conditions

$$\begin{aligned}&\sum_{e=1}^{N} \begin{bmatrix} \int_{\partial\Omega_e} [\boldsymbol{L}^e]^{\mathrm{T}}[\boldsymbol{n}^e]^{\mathrm{T}}[\boldsymbol{P}^m]\,\mathrm{d}\Omega & \boldsymbol{0} \\ -\int_{\partial\Omega_c} [\boldsymbol{L}^c]^{\mathrm{T}}[\boldsymbol{n}^c]^{\mathrm{T}}[\boldsymbol{P}^m]\,\mathrm{d}\Omega & \int_{\partial\Omega_c} [\boldsymbol{L}^c]^{\mathrm{T}}[\boldsymbol{n}^c]^{\mathrm{T}}[\boldsymbol{P}^c]\,\mathrm{d}\Omega \\ \boldsymbol{0} & -\int_{\partial\Omega_{\mathrm{cr}}} [\mathrm{L}^{\mathrm{cr}}]^{\mathrm{T}}[\boldsymbol{n}^{cr}]^{\mathrm{T}}[\boldsymbol{P}^c]\,\mathrm{d}\Omega \end{bmatrix} \begin{Bmatrix} \boldsymbol{\beta}^m + \Delta\boldsymbol{\beta}^m \\ \boldsymbol{\beta}^c + \Delta\boldsymbol{\beta}^c \end{Bmatrix}\\ &= \sum_{e=1}^{N} \begin{Bmatrix} \int_{\Gamma_{tm}} [\boldsymbol{L}^e]^{\mathrm{T}}\{\bar{\boldsymbol{t}} + \Delta\bar{\boldsymbol{t}}\}\,\mathrm{d}\Omega \\ \{\boldsymbol{0}\} \\ \{\boldsymbol{0}\} \end{Bmatrix}\end{aligned} \tag{22}$$

Eqs. (21) and (22) along with the constitutive relations can now be used to solve for the unknown stress coefficients and nodal displacements.

2.3. Constitutive relations and damage initiation criterion

The inclusion phase is assumed to be brittle and is modeled as a linear elastic material. The matrix phase on the other hand projects ductile behavior and is modeled by small deformation elasto–plastic constitutive relation using J_2 flow theory with isotropic hardening. In his model, an additive decomposition of the strain increments $\Delta\boldsymbol{\epsilon}$ into an elastic part $\Delta\boldsymbol{\epsilon}^{\mathrm{e}}$ and a plastic part $\Delta\boldsymbol{\epsilon}^{\mathrm{pl}}$ is assumed.

$$\Delta\boldsymbol{\epsilon} = \Delta\boldsymbol{\epsilon}^{\mathrm{e}} + \Delta\boldsymbol{\epsilon}^{\mathrm{pl}} \tag{23}$$

where $\Delta\boldsymbol{\epsilon}^{\mathrm{e}}$ is obtained through the linear elastic relationship, and $\Delta\boldsymbol{\epsilon}^{\mathrm{pl}}$ is obtained through the integration of the associated flow rule. Details of the Backward Euler procedure used for integration is presented in [25,20]. Numerical implementation requires computation of tangent operators through linearized forms of the constitutive relations. If $\mathrm{d}\boldsymbol{\epsilon}$ is the first-order correction to the current strain increment $\Delta\boldsymbol{\epsilon}$, and $\mathrm{d}\boldsymbol{\sigma}$ is the corresponding correction to the stress increment $\Delta\boldsymbol{\sigma}$, the fourth-order elastic–plastic compliance tensor (or tangent operator) $\boldsymbol{S}$ is given by the relation

$$\mathrm{d}\boldsymbol{\epsilon} = \boldsymbol{S} : \mathrm{d}\boldsymbol{\sigma}$$

The elastic part of this equation is expressed as

$$\mathrm{d}\boldsymbol{\epsilon}^{\mathrm{e}} = \boldsymbol{S}_{\mathrm{e}} : \mathrm{d}\boldsymbol{\sigma}$$

where $\boldsymbol{S}_e$ is the linear-elastic compliance tensor written as

$$\boldsymbol{S}_{\mathrm{e}} = \frac{1+\nu}{E}\boldsymbol{I} - \frac{\nu}{E}\boldsymbol{\delta}\otimes\boldsymbol{\delta} \tag{24}$$

$\boldsymbol{I}$ in this equation is the fourth-order identity tensor. The plastic part of the strain correction $\mathrm{d}\boldsymbol{\epsilon}^{\mathrm{pl}}$ however requires a first-order approximation $\mathrm{d}\lambda$ to the current flow parameter $\Delta\lambda$, which for J_2 flow theory (see [26]), takes the form

$$\mathrm{d}\boldsymbol{\epsilon}^{\mathrm{pl}} = \frac{9}{4H}\frac{(\boldsymbol{\sigma}+\Delta\boldsymbol{\sigma})'\otimes(\boldsymbol{\sigma}+\Delta\boldsymbol{\sigma})'}{(\sigma_{\mathrm{eff}}^{p+1})^2} : \mathrm{d}\boldsymbol{\sigma} = \boldsymbol{S}_{\mathrm{pl}} : \mathrm{d}\boldsymbol{\sigma} \tag{25}$$

where H is a linearized hardening modulus. The elasto–plastic tangent operator $\boldsymbol{S}$ is obtained by adding Eqs. (24) and (25) as

$$\boldsymbol{S} = \boldsymbol{S}_{\mathrm{e}} + \boldsymbol{S}_{\mathrm{pl}} \tag{26}$$

A linearized form of the incremental complementary energy functional ΔB can now be expressed in terms of the tangent operator as

$$\mathrm{d}B(\boldsymbol{\sigma}, \mathrm{d}\boldsymbol{\sigma}) = \frac{1}{2}\mathrm{d}\boldsymbol{\sigma} : \boldsymbol{S} : \mathrm{d}\boldsymbol{\sigma} \tag{27}$$

Note that the elastic–plastic tangent operator $\boldsymbol{S}$ in Eq. (26) is positive definite since its components are individually positive definite. Both plane stress and plane strain conditions are solved in an iterative manner.

2.3.1. Particle cracking criterion

Microstructural damage by complete particle cracking and splitting is initiated by a criterion based on the maximum principal stress, also known as the Rankine criterion for brittle materials. In this criterion, a crack is initiated at a point when the maximum principal stress in tension exceeds a critical failure stress σ_{cr}. In the computational procedure, once the principal tensile stress at any point in the inclusion reaches this critical value σ_{cr}, complete particle cracking or splitting is assumed by a blunt elliptical crack running through the inclusion. In the case of complete particle cracking, the crack tip coincides with the interface, while it extends into the matrix in the case of particle splitting. The orientation of the crack is normal to the direction of maximum principal stress. In actual computations, more than one point may have exceeded the critical σ_{cr} value during increment, which poses problems with respect to the location of the crack. This is averted by a weighted averaging method, that determines a unique location for the crack. If $\sigma_I^c(x, y)$ corresponds to all values of maximum tensile principal stress larger than σ_{cr} in the inclusion, the location of the crack is determined as

$$\begin{aligned} x_{\mathrm{damage}} &= \frac{\sum x \dfrac{\sigma_I^c(x, y)}{\sigma_{\mathrm{cr}}}}{\sum \dfrac{\sigma_I^c(x, y)}{\sigma_{\mathrm{cr}}}} \quad \forall\, [\sigma_I^c(x, y) \geq \sigma_{\mathrm{cr}}] \\ y_{\mathrm{damage}} &= \frac{\sum y \dfrac{\sigma_I^c(x, y)}{\sigma_{\mathrm{cr}}}}{\sum \dfrac{\sigma_I^c(x, y)}{\sigma_{\mathrm{cr}}}} \quad \forall\, [\sigma_I^c(x, y) \geq \sigma_{\mathrm{cr}}] \end{aligned} \tag{28}$$

The crack is oriented at right angles to the principal stress directions at $(x_{\mathrm{damage}}, y_{\mathrm{damage}})$, and its length determined from the orientation and inclusion shape and size.

Several experimental studies conducted for metal matrix composites [17–19], suggests that critical stress for particle fracturing depends not only on material, but has a strong relation to the particle size itself. SEM micrographs of damaged composites show that larger particles tend to fracture at lower macroscopic load levels than smaller particles. Curtin [27], Amornskhai [28], among others, have developed a fracture mechanics based damage criterion, in which the fracture strength of individual particles are derived based on their size as well as material properties. Particles in these models are assumed to contain flaws, and the critical stress to fracture is determined based on mode-I fast fracture of these flaws. Consider a particle of area A, whose characteristic length is given by the diameter of an equivalent circle, viz. $D = \sqrt{4A/\pi}$. The initial flaw size c in the particle is assumed to be a fraction of its equivalent diameter through $c = eD$, where e is chosen to be ~5–15% in this study. Thus, for mode-I fracture, the critical load to fracture σ_{cr} is related to the fracture toughness K_{IC} through the relation:

$$\sigma_{\mathrm{cr}} = \frac{K_{IC}}{\sqrt{c\pi}} \tag{29}$$

K_{IC} is an assumed material constant in this relation. It is clear that larger particles (with larger initial flaws) will fracture at smaller critical loads according to this relation.

2.4. Method of solution

An iterative solution process is invoked to evaluate the stresses from Eq. (21), given the nodal displacement increments $\{\Delta \boldsymbol{q}\}\{\Delta \boldsymbol{q}'\}$ and $\{\Delta \boldsymbol{q}''\}$. Let $\{\mathrm{d}\boldsymbol{\beta}\}^i$ correspond to the correction to $\Delta\boldsymbol{\beta}$'s in the ith iteration, i.e.

$$\begin{aligned} \{\Delta\boldsymbol{\beta}^m\} &= \{\Delta\boldsymbol{\beta}^m\}^i + \{\mathrm{d}\boldsymbol{\beta}^m\}^i \\ \{\Delta\boldsymbol{\beta}^c\} &= \{\Delta\boldsymbol{\beta}^c\}^i + \{\mathrm{d}\boldsymbol{\beta}^c\}^i \end{aligned}$$

The kinematic equation (21) may then be linearized with respect to $\Delta\boldsymbol{\beta}$ to yield

$$\begin{bmatrix} \boldsymbol{H}_m & \boldsymbol{0} \\ \boldsymbol{0} & \boldsymbol{H}_c \end{bmatrix} \begin{Bmatrix} \mathrm{d}\boldsymbol{\beta}^m \\ \mathrm{d}\boldsymbol{\beta}^c \end{Bmatrix}^i = \begin{bmatrix} \boldsymbol{G}_e & -\boldsymbol{G}_{cm} & \boldsymbol{0} \\ \boldsymbol{0} & \boldsymbol{G}_{cc} & -\boldsymbol{G}_{\mathrm{cr}} \end{bmatrix} \begin{Bmatrix} \boldsymbol{q} + \Delta\boldsymbol{q} \\ \boldsymbol{q}' + \Delta\boldsymbol{q}' \\ \boldsymbol{q}'' + \Delta\boldsymbol{q}'' \end{Bmatrix} \tag{30}$$

$$- \begin{Bmatrix} \displaystyle\int_{\Omega_m} [\boldsymbol{P}^m]^{\mathrm{t}} \{\boldsymbol{\epsilon} + \Delta\boldsymbol{\epsilon}\}^i \, \mathrm{d}\Omega \\ \displaystyle\int_{\Omega_c} [\boldsymbol{P}^c]^{\mathrm{t}} \{\boldsymbol{\epsilon} + \Delta\boldsymbol{\epsilon}\}^i \, \mathrm{d}\Omega \end{Bmatrix} \tag{31}$$

where matrices $[\boldsymbol{H}_m]$, $[\boldsymbol{H}_c]$, $[\boldsymbol{G}_e]$, $[\boldsymbol{G}_{cm}]$, $[\boldsymbol{G}_{cc}]$ are written as

$$
\begin{aligned}
&[\boldsymbol{H}_m] = \int_{\Omega_m} [\boldsymbol{P}^m]^{\mathrm{T}}[\boldsymbol{S}][\boldsymbol{P}^m]\,\mathrm{d}\Omega\,, \qquad [\boldsymbol{H}_c] = \int_{\Omega_c} [\boldsymbol{P}^c]^{\mathrm{T}}[\boldsymbol{S}][\boldsymbol{P}^c]\,\mathrm{d}\Omega \\
&[\boldsymbol{G}_e] = \int_{\partial\Omega_e} [\boldsymbol{P}^m]^{\mathrm{T}}[\boldsymbol{n}^e][\boldsymbol{L}^e]\,\mathrm{d}\Omega\,, \qquad [\boldsymbol{G}_{cm}] = \int_{\partial\Omega_c} [\boldsymbol{P}^m]^{\mathrm{T}}[\boldsymbol{n}^c][\boldsymbol{L}^c]\,\mathrm{d}\Omega[\boldsymbol{G}_{cc}] = \int_{\partial\Omega_c} [\boldsymbol{P}^c]^{\mathrm{T}}[\boldsymbol{n}^c][\boldsymbol{L}^c]\,\mathrm{d}\Omega \\
&[\boldsymbol{G}_{\mathrm{cr}}] = \int_{\partial\Omega_{\mathrm{cr}}} [\boldsymbol{P}^c]^{\mathrm{T}}[\boldsymbol{n}^{\mathrm{cr}}][\boldsymbol{L}^{\mathrm{cr}}]\,\mathrm{d}\Omega
\end{aligned}
\tag{32}
$$

and $[\boldsymbol{S}(x, y)]$ is the instantaneous elastic–plastic tangent compliance tensor as derived in Eq. (26). The linearized matrix equation (31) is solved for stress coefficients using a Quasi-Newton iterative solution procedure [29].

Proceeding in the same way, with known stress increments let $\{\mathrm{d}\boldsymbol{q}\}^j$ correspond to the correction in $\{\Delta\boldsymbol{q}\}$ in the jth iteration of the linearized weak form of the global traction reciprocity equation (22), i.e.

$$
\begin{aligned}
&\{\Delta\boldsymbol{q}\} = \{\Delta\boldsymbol{q}\}^j + \{\mathrm{d}\boldsymbol{q}\}^j \\
&\{\Delta\boldsymbol{q}'\} = \{\Delta\boldsymbol{q}'\}^j + \{\mathrm{d}\boldsymbol{q}'\}^j \\
&\{\Delta\boldsymbol{q}''\} = \{\Delta\boldsymbol{q}''\}^j + \{\mathrm{d}\boldsymbol{q}''\}^j
\end{aligned}
\tag{33}
$$

Substituting Eq. (31) in (22) and taking variations with respect to the displacement increments $\{\Delta\boldsymbol{q}\}$, $\{\Delta\boldsymbol{q}'\}$ and $\{\Delta\boldsymbol{q}''\}$ yields the following matrix equations:

$$
\begin{aligned}
&\sum_{e=1}^{N} [\boldsymbol{G}]^{\mathrm{T}}[\boldsymbol{H}]^{-1}[\boldsymbol{G}]\begin{Bmatrix} \mathrm{d}\boldsymbol{q} \\ \mathrm{d}\boldsymbol{q}' \\ \mathrm{d}\boldsymbol{q}'' \end{Bmatrix}^j = \sum_{e=1}^{N} \begin{Bmatrix} \int_{\Gamma_{tm}} [\boldsymbol{L}^m]^{\mathrm{T}}\{\bar{\boldsymbol{t}} + \overline{\Delta\boldsymbol{t}}\}\,\mathrm{d}\Omega \\ \boldsymbol{0} \\ \boldsymbol{0} \end{Bmatrix} \\
&\quad - \sum_{e=1}^{N} \begin{bmatrix} \int_{\partial\Omega_e} [\boldsymbol{L}^e]^{\mathrm{T}}[\boldsymbol{n}^e]^{\mathrm{T}}[\boldsymbol{P}^m]\,\mathrm{d}\Omega & \boldsymbol{0} \\ -\int_{\partial\Omega_e} [\boldsymbol{L}^c]^{\mathrm{T}}[\boldsymbol{n}^c]^{\mathrm{T}}[\boldsymbol{P}^m]\,\mathrm{d}\Omega & \int_{\partial\Omega_c} [\boldsymbol{L}^c]^{\mathrm{T}}[\boldsymbol{n}^c]^{\mathrm{T}}[\boldsymbol{P}^c]\,\mathrm{d}\Omega \\ \boldsymbol{0} & -\int_{\partial\Omega_{\mathrm{cr}}} [\boldsymbol{L}^{\mathrm{cr}}]^{\mathrm{T}}[\boldsymbol{n}^{\mathrm{cr}}]^{\mathrm{T}}[\boldsymbol{P}^c]\,\mathrm{d}\Omega \end{bmatrix} \begin{Bmatrix} \boldsymbol{\beta}^m + \Delta\boldsymbol{\beta}^m \\ \boldsymbol{\beta}^c + \Delta\boldsymbol{\beta}^c \end{Bmatrix}^j
\end{aligned}
$$

or, in standard finite element notation

$$
\begin{aligned}
&\sum_{e=1}^{N} [\boldsymbol{K}_e]\{\mathrm{d}\boldsymbol{u}\}^j = \sum_{e=1}^{N} \{\boldsymbol{f}_e\} \\
&\quad - \sum_{e=1}^{N} \begin{bmatrix} \int_{\partial\Omega_e} [\boldsymbol{L}^e]^{\mathrm{T}}[\boldsymbol{n}^e]^{\mathrm{T}}[\boldsymbol{P}^m]\,\mathrm{d}\Omega & \boldsymbol{0}\,. \\ -\int_{\partial\Omega_e} [\boldsymbol{L}^c]^{\mathrm{T}}[\boldsymbol{n}^c]^{\mathrm{T}}[\boldsymbol{P}^m]\,\mathrm{d}\Omega & \int_{\partial\Omega_c} [\boldsymbol{L}^c]^{\mathrm{T}}[\boldsymbol{n}^c]^{\mathrm{T}}[\boldsymbol{P}^c]\,\mathrm{d}\Omega \\ \boldsymbol{0} & -\int_{\partial\Omega_{\mathrm{cr}}} [\boldsymbol{L}^{\mathrm{cr}}]^{\mathrm{T}}[\boldsymbol{n}^{\mathrm{cr}}]^{\mathrm{T}}[\boldsymbol{P}^c]\,\mathrm{d}\Omega \end{bmatrix} \begin{Bmatrix} \boldsymbol{\beta}^m + \Delta\boldsymbol{\beta}^m \\ \boldsymbol{\beta}^c + \Delta\boldsymbol{\beta}^c \end{Bmatrix}^j
\end{aligned}
\tag{34}
$$

The linearized global traction reciprocity condition in Eq. (34) is used to iteratively solve for the nodal displacement increments.

2.5. *Numerical aspects of the Voronoi cell element implementation*

Effective implementations of the Voronoi cell finite element formulation requires great caution in avoiding numerical instability for the various matrix systems developed in the previous sections. For example, optimal conditioning of matrices $[\boldsymbol{H}_m]$ and $[\boldsymbol{H}_c]$ is obtained by using a scaled representation of the stress functions as outlined in Sections 2.2.1 and 2.2.2. Suppression of rigid body modes on the inclusion interface, and spurious kinematic modes of deformation due to low element energy are essential, and have been discussed in [20,21]. Accurate *domain integration* of Eq. (32) to evaluate $[\boldsymbol{H}_m]$ and $[\boldsymbol{H}_c]$ is also crucial to the convergence of this method. Numerical integration of these functions are performed by dividing the matrix domain Ω_m and the inclusion domain Ω_c into quadrilaterals and triangles and applying Gaussian quadrature formulae. For undamaged Voronoi cells, the inclusion domain Ω_c is a simply connected convex area whose division is easily accomplished. The matrix domain Ω_m, however, is multiply connected and a general algorithm for subdividing it into convex quadrilaterals is detailed in [25]. For polynomial stress functions, $[\boldsymbol{H}_c]$ matrix is also polynomial functions of scaled coordinates (ξ, η). Numerical integration is performed by using Gaussian quadrature rule on the divided quadrilaterals/triangles, with appropriate number of Gauss points.

The $[\boldsymbol{H}_m]$ matrix, on the other hand, comprises of both polynomial and reciprocal terms. Of these, the sharpest gradients are exhibited by the reciprocal terms and the maximum reciprocal order in $[\boldsymbol{H}_m]$ may be shown to be $\mathcal{O}(1/(f^2(M+n+1))$. Since the reciprocal terms vary rapidly near the interface from a high value, a large number of subdivisions with a larger number of integration points are concentrated near the interface to accurately integrate functions of the order $\mathcal{O}(1/(f^{2(M+n+1)}))$. An adaptive scheme is employed for subdividing individual quadrilaterals in the matrix domain Ω_e to enhance accuracy and is discussed in [25].

With the introduction of the crack surface in the Voronoi element topology, two essential features are altered in the discretization procedure. First, for the damaged Voronoi cells sharpest stress gradients arise from reciprocal terms $1/f_{\mathrm{cr}}^{p+q+i-1}$ and consequently the mapping function f_{cr} of the crack boundary is used as a major criterion in the matrix discretization. Secondly, the inclusion domain is no longer simply connected and hence the subdivision into quadrilaterals follows that of the matrix domain discussed earlier.

3. Numerical examples for validation of the Voronoi cell FE model

The effectiveness of the Voronoi cell finite element model in stress analysis of heterogeneous materials with damage is verified by comparison with results of conventional finite element analyses, as well as with published results in the literature.

3.1. A square homogeneous domain with an elliptical crack

A square domain of a hardening matrix with an elliptical crack is loaded in uniaxial tension to a macroscopic tensile strain $\bar{\epsilon}_{yy} = 0.5\%$, as shown in Fig. 2a. Results of VCFEM simulation are compared with the Hutchinson–Rice–Rosengren (HRR) field [30], that is generated by an asymptotic analysis of a sharp crack in a nonlinear elastic matrix. The elliptical crack has an aspect ratio of $a/b = 100$ and $a/L = \frac{1}{10}$. Material properties are as follows: Young's modulus $E = 50$ units, Poisson's ratio $\nu = 0.33$; post yield behavior (Ramberg–Osgood law) $\sigma_m = \sigma_0(\epsilon_m^p/\alpha\epsilon_0)^{1/n}$, where the initial flow stress of the matrix $\sigma_0 = 1$ unit, ϵ_0 is the strain at yield $(\epsilon_0 = \sigma_0/E)$, and material parameter $\alpha = 0.02$. Three values of strain hardening exponent, viz. $n = 1$, 3 and 13 are considered.

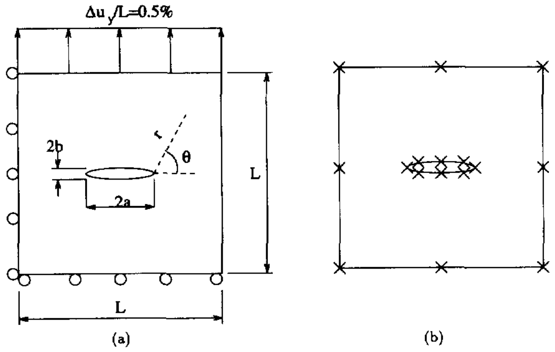

Fig. 2. (a) A square homogeneous matrix with an elliptical crack; (b) VCFE mesh (×) refers to the node locations.

The Voronoi cell mesh consists of only one element, for which the boundary is discretized using 8 nodes (marked with '×') with linear displacement interpolation, as shown in Fig. 2b. The elliptical crack is modeled using 8 nodes, with quadratic line elements between the nodes. Two sides of the domain are roller supported implying symmetry, while the other two sides are kept straight implying periodicity. The matrix stress function consists of 12 polynomial terms (4th order polynomial, i.e. $p+q=2\cdots 4$) and 36 reciprocal terms based on a conformal map of the elliptical crack (3 reciprocal terms for each polynomial exponent from 2 to 4, i.e. $i=p+q\cdots p+q+2\ \forall\ p+q\in[2,4]$). The analysis is carried out under both plane stress and plane strain conditions. Sanders [31] and Rice [32] have proposed that under the assumptions of small scale yielding, the elastic–plastic J integral for contours that are far from the crack-tip, have the same values as their linear elastic counterparts. The linear elastic J integrals for finite crack sizes has been derived in [31], as $J_{\text{plane stress}}=\bar{\sigma}_{yy}^2 L/E\tan \pi a/L$, and $J_{\text{plane strain}}=(1-\nu^2)J_{\text{plane stress}}$ where $\bar{\sigma}_{yy}$ is the far field macroscopic stress. The macroscopic stress is computed as the volume averaged stress for the entire domain. Variations of the J integral with increased macroscopic tension under plane strain and plane stress conditions are depicted in Fig. 3(a,b) respectively for $n=1$, 3 and 13. VCFE results are in excellent agreement with the theoretical values for all ns up to $\bar{\sigma}_{yy}=0.14\sigma_0$. At higher macroscopic load levels, the VCFE depicts higher values of J integrals for the higher ns, indicating a departure from small scale yielding solution.

The asymptotic HRR field predicts that at a constant angle θ (see Fig. 4(a)) the individual components of the stresses vary as

$$\sigma_{ij}(r,\theta)=\frac{K}{r^{s}}\hat{\sigma}_{ij}(\theta)\,,\qquad s=\frac{1}{n+1} \tag{35}$$

where K is the stress intensity factor. Fig. 4(a) show the stress variation at $\theta=0$ for a strain hardening exponent $n=3$ under plane stress conditions as a function of the radial distance. The HRR field predictions are plotted by equating the VCFEM stresses at $r/b=10$ to that in Eq. (35) for evaluating $K\hat{\sigma}_{ij}(\theta)|_{\theta=0}$. These results show excellent correlation with the HRR field until near the crack tip ($r/b=1.0$). For lower radial distances, the stress component σ_{rr} begins to drop. The decrease in radial component of the stress is because the traction $t_r=\sigma_{rr}$ at the tip of the elliptical crack vanishes to satisfy zero traction boundary conditions at $r/b=0$. The drop in the radial component σ_{rr} triggers a fall in the hoop component $\sigma_{\theta\theta}$ at a radial distance $r/b=0.2$. These results are in qualitative agreement with finite element calculations by McMeeking [33] for blunt cracks. The angular variation of the Von Mises stress σ_m and shear stress $\sigma_{r\theta}$ at $r/b=3$ are compared with the HRR field in Figs. 4(b) and 5(a), respectively. The plots are in good agreement with their respective HRR counterparts upto an angle of $\theta=90°$. However, for $\theta>90°$, there is a deviation from HRR results. This may be attributed to the blunt nature of the elliptical crack, since radial lines intersects the elliptical crack on the blunt surface where zero traction boundary conditions exist on the crack surface. Finally, the effective plastic strain distribution in a small region ($10b\times 8b$ window) near the crack tip is shown in Fig. 5(b). It can be seen from this plot that the

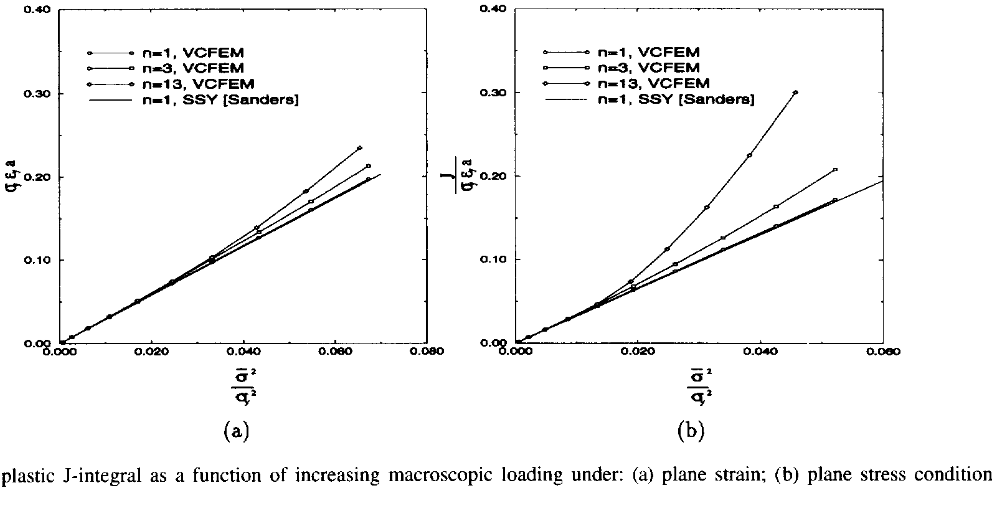

(a) (b)

Fig. 3. Elastic plastic J-integral as a function of increasing macroscopic loading under: (a) plane strain; (b) plane stress conditions.

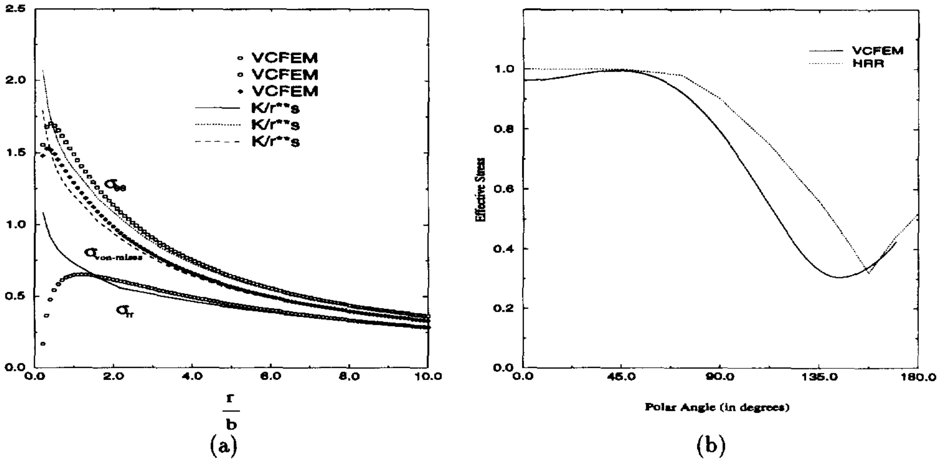

(a) (b)

Fig. 4. Variation of (a) cylindrical stress components with radial distance at $\theta = 0$; (b) effective stress with the polar angle at $r/b = 1$ for a hardening exponent $n = 3$, plane stress calculations.

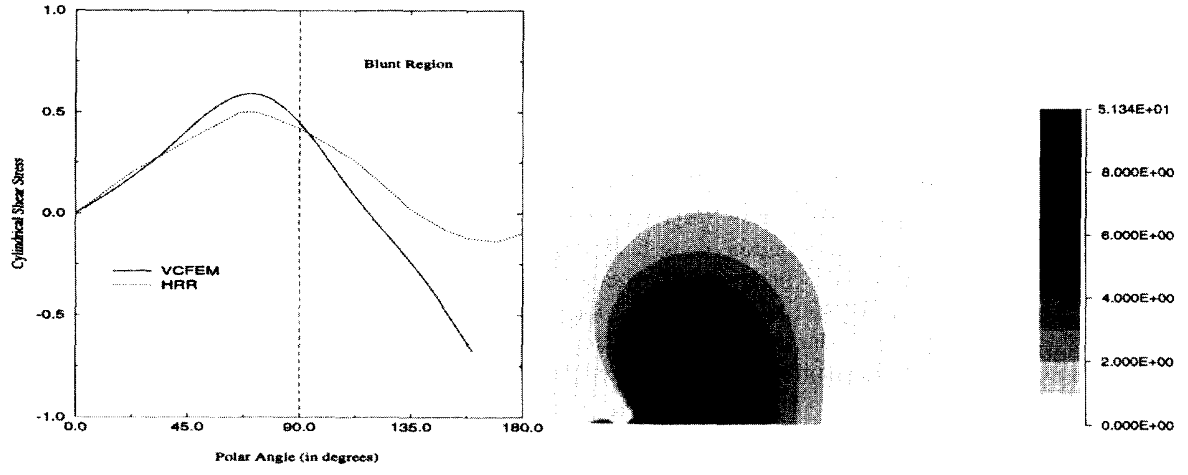

(a) (b)

Fig. 5. (a) Variation of cylindrical shear stress component $\sigma_{r\theta}$ with the polar angle at $r/b = 1$; (b) effective plastic strain (%) at the crack tip for hardening exponent $n = 3$, plane stress calculations.

plastic straining extends ahead of the crack tip for the plane stress case. Similar observations have been made by Hutchinson [30] and Rice [32].

3.2. Comparison with commercial code for composite with pre-existing crack

A unit cell, corresponding to an uniformly distributed composite microstructure with a pre-cracked circular inclusion is analyzed in this example. VCFEM results are compared with those generated by the general purpose FEA code ABAQUS [34]. The volume fraction of the inclusion is $V_f = 20\%$ and the elliptical crack is modeled with an aspect ratio of $a/b = 10$ as shown in Fig. 6(a). The unit cell is monotonically loaded in uniaxial tension, perpendicular to the crack surface, to an overall strain of $\bar{\epsilon}_{yy} = 0.5\%$. Periodicity conditions are enforced on the surface $x = L/2$ by constraining it to remain vertical and straight, and the analysis is conducted under plane strain conditions. The matrix material is assumed to be a ductile Al-3.5% Cu alloy with elastic–plastic behavior characterized as Young's modulus $E = 72$ GPa, Poisson's ratio $\nu = 0.32$; post yield behavior $\sigma_m = \sigma_0(\epsilon^p_m/\epsilon_0 + 1)^N$, with $\sigma_0 = 175$ MPa, $N = 0.2$, and $\epsilon_0 = \sigma_0/E$ is the uniaxial strain at yield.

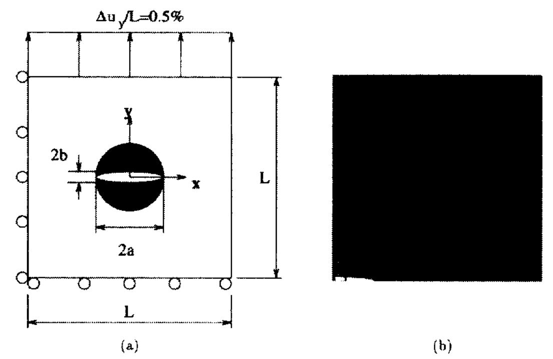

Fig. 6. (a) VCFE mesh and (b) ABAQUS meshes for a uniformly distributed composite with a pre-existing crack in the circular inclusion ($V_f = 20\%$).

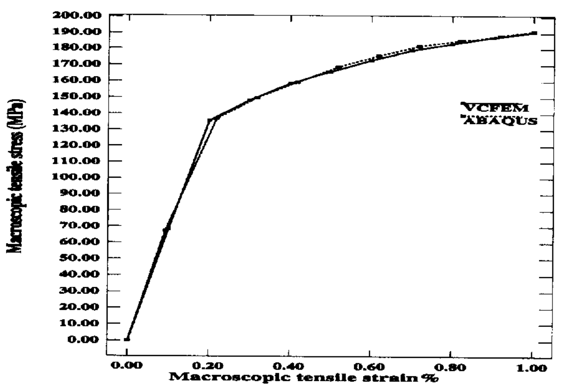

Fig. 7. Macroscopic stress–strain response of unit cell with a pre-existing crack in a circular inclusion of $V_f = 20\%$.

The brittle inclusion is assumed to be of SiC, with elastic properties as Young's modulus $E = 450$ GPa, Poisson's ratio $\nu = 0.17$.

The single element in the VCFE mesh (Fig. 6(a)) is discretized into 8 linear elements on the boundary, 8 quadratic line elements on the crack boundary and 12 quadratic elements on the inclusion boundary. The inclusion stress function is generated using 25 polynomial terms (6th order polynomial stress function, i.e. $p + q = 2 \cdots 6$) and 36 reciprocal terms with f_{cr} (3 reciprocal terms for each polynomial exponent from 2 to 4, i.e. $i = p + q \cdots p + q + 2\ \forall\ p + q \in [2, 4]$). The matrix stress function has an additional 9 reciprocal terms due to f (3 reciprocal terms for the polynomial exponent 2, i.e. $i = p + q \cdots p + q + 2\ \forall\ p + q = 2$). The corresponding ABAQUS mesh is made up of 1465 8-noded quadratic elements, with 6431 nodes as shown in Fig. 6(b). The macroscopic stress–strain response in Fig. 7 depicts a good match between VCFEM and ABAQUS. Microscopic stress distribution along horizontal lines at different vertical distances from the crack tip, shown in Fig. 8, exhibit good concurrence between VCFEM and ABAQUS. The peak stress in the stiffer inclusion (~13 000 MPa) at the matrix/inclusion interface near the crack tip is significantly higher than that in the matrix (~245 MPa). The inclusion peak stress decays with increasing distance from the crack tip. This phenomenon, known crack tip amplification, has been reported for bi-material interfaces by Sugimura et al. [12].

3.3. Diagonally packed square inclusions with a pre-existing crack

This problem, involving stress analysis in a diagonally packed composite with pre-cracked square inclusions, has been studied by Finot et al. [13]. The representative material element (RME) consists of two square shaped SiC inclusions in an Al-3.5% Cu matrix with a volume fraction $V_f = 20\%$, and are loaded vertically as shown in Fig. 9. The inclusions are arranged in square diagonal pattern, and the corresponding Voronoi mesh of two elements is shown in Fig. 9. The matrix material is and Al-3.5% Cu alloy with properties: Young's modulus $E = 72$ GPa, Poisson's ratio $\nu = 0.32$; Post yield behavior (Power law hardening) $\sigma_m = \sigma_0(\epsilon_m^p / \epsilon_0 + 1)^N$ with $\sigma_0 = 175$ MPa, and $N = 0.2$. The inclusions are of SiC with Young's modulus $E = 450$ GPa and Poisson's ratio $\nu = 0.2$.

In accordance with definitions used in [13], 0% damage corresponds to the representative material element (RME) with both inclusions intact, 50% to the RME with one cracked inclusion, and 100% damage refers to RME with both inclusions cracked. Elliptical cracks in the VCFEM analysis are assigned an aspect ratio $a/b = 10$, and a parameter $d = (\text{Crack Length})/(\text{Inclusion Dimension})$ distinguishes between complete cracking and splitting of inclusions. A fully cracked inclusion corresponds to a value $d = 1$, for which the crack terminates at the inclusion–matrix interface, whereas splitting is represented by $d = 1.004$ for which the crack tip has moved slightly into the matrix. For 0% damage, the matrix stress fields are represented by a 61 term expansion and the inclusion stress field by a 25 term expansion. For 50% and 100% damage, the matrix and the inclusion stress fields have an additional 36 terms based on conformal mapping of the elliptical crack ($i = p + q \cdots p + q + 2\ \forall\ p + q = 2 \cdots 4$). The function f in the matrix reciprocal terms is created by a Fourier series transformation of the square interface for this problem.

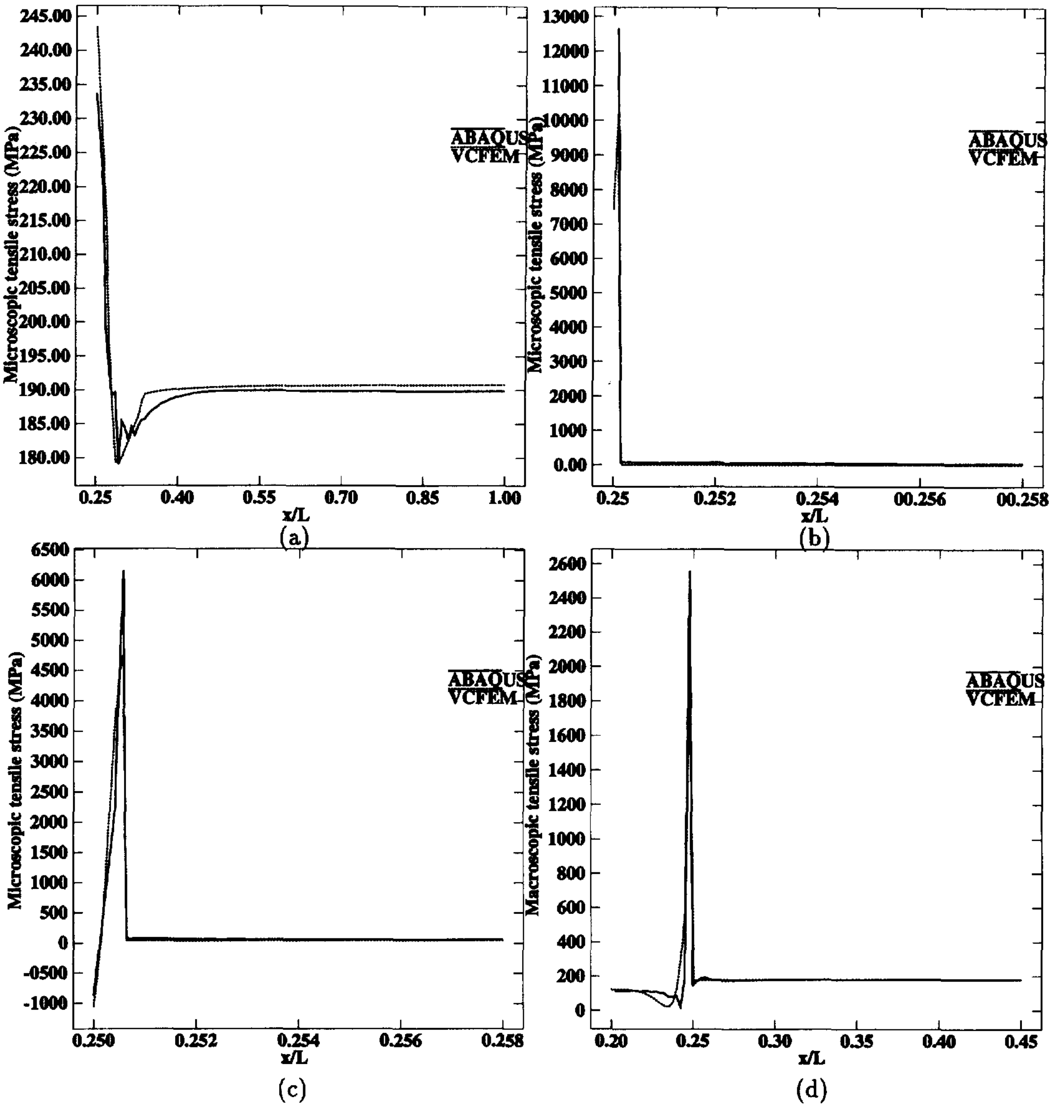

Fig. 8. Microscopic tensile stress distribution along: (a) $y/b = 0$; (b) $y/b = 0.1$; (c) $y/b = 0.25$; (d) $y/b = 0.5$ for unit cell with a pre-existing crack in a circular inclusion of $V_f = 20\%$.

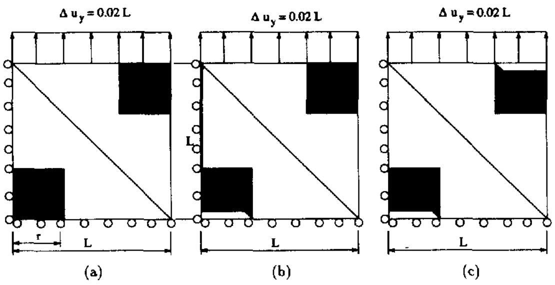

Fig. 9. Representation and VCFEM mesh for RME with $V_f = 20\%$ cracked square inclusions. (a) 0% damage; (b) 50% damage; (c) 100% damage.

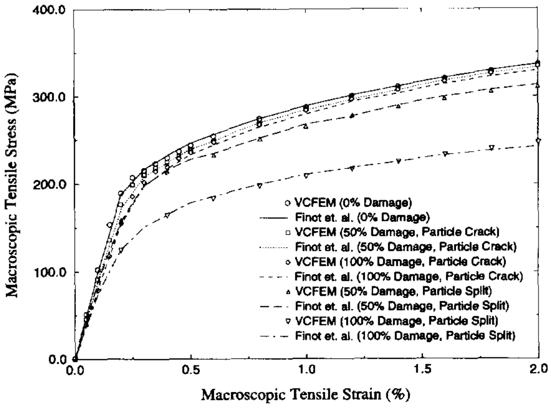

Fig. 10. Macroscopic stress–strain response for RMEs with $V_f = 20\%$ cracked square inclusions.

Overall stress–strain response is computed by taking volumetric averages of respective microscopic variables, and are compared with those of [13] in Fig. 10. Excellent agreement is recorded at all levels of macroscopic strain both for particle cracking and splitting. The stress carrying capacity of the material element reduces considerably with the transition from full particle cracking to particle splitting. This is because as the crack grows beyond the interface, there is no load transfer between the two halves of the inclusions and consequently the entire load has to be carried by the matrix material and the remainder of undamaged particles.

Contour plots of the effective plastic strains for the cracked and split microstructures at $\bar{\epsilon}_{yy} = 2\%$ are presented in Figs. 11 and 12, respectively. Contour plots for split particles show that portions above the particles have drastically reduced plastic strains, since they no longer carry any of the load. It is also important to note that in the case of particle splitting, a considerably larger plastic strain accumulates near the crack tip. Also, plastic strains tend to flow in the form of ligaments from one crack tip to the next, causing bands of strain localization. Similar observations have been made in [13] for axisymmetric particles.

3.4. Effect of damage level on stress carrying capacity

In this example, the effect of selectively damaged particles on the overall material response is analyzed in plane strain and compared with axisymmetric predictions made in [10], and Brockenbrough and Zok [35].

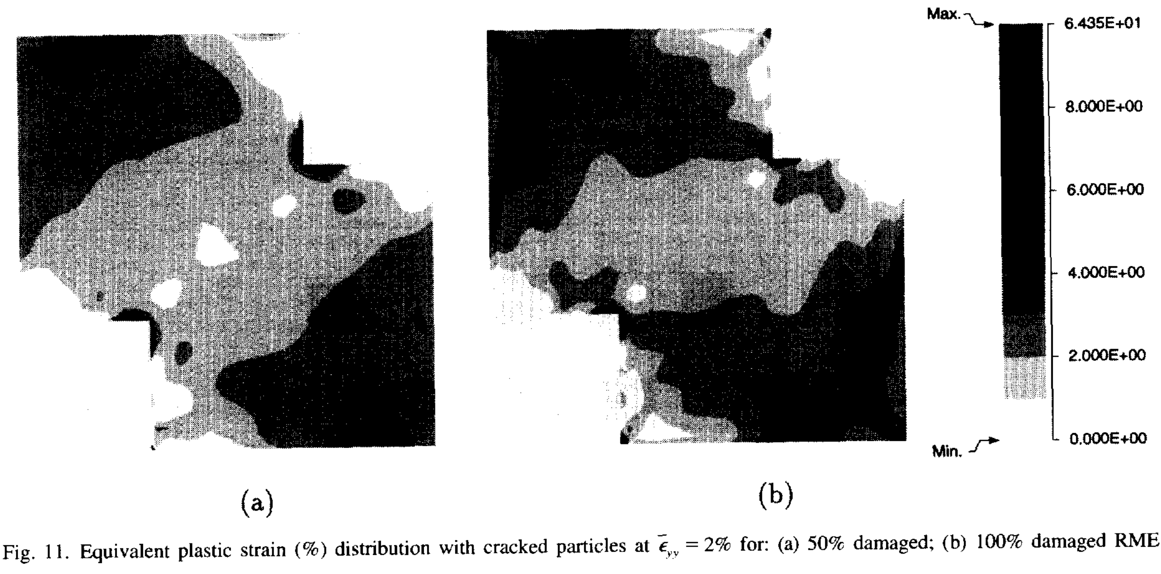

Fig. 11. Equivalent plastic strain (%) distribution with cracked particles at $\bar{\epsilon}_{yy} = 2\%$ for: (a) 50% damaged; (b) 100% damaged RME.

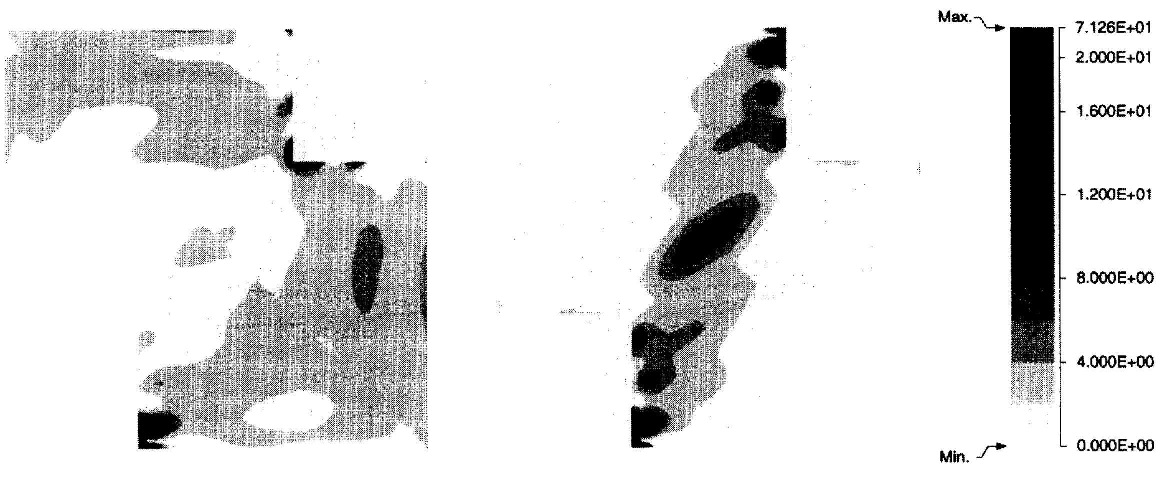

(a) (b)

Fig. 12. Equivalent plastic strain (%) distribution with split particles at $\bar{\epsilon}_{yy} = 2\%$ for: (a) 50% damaged; (b) 100% damaged RME.

Complete particle splitting is considered, i.e. $d = 1.004$. Fig. 13 shows the various levels of damage in representative material elements that are analyzed for up to a maximum vertical strain of $\bar{\epsilon}_{yy} = 0.5\%$. Periodicity conditions are enforced on the boundaries. A parameter ρ = (number of damaged particles)/(total number of particles), is used as an indicator of the extent of damage. Five values of $\rho = 0, 0.25, 0.33, 0.375$ and 1 are considered. The matrix material is ductile with the properties: Young's modulus $E = 70$ GPa, Poisson's ratio

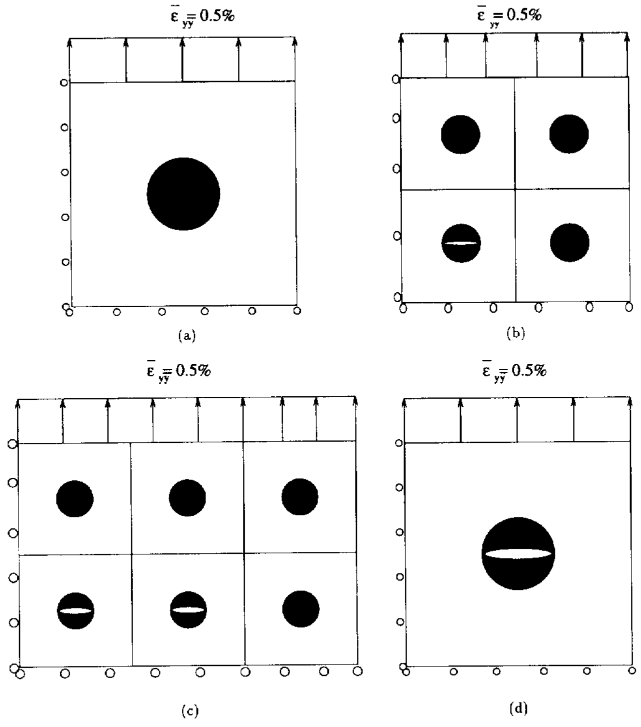
$\bar{\varepsilon}_{yy} = 0.5\%$
$\bar{\varepsilon}_{yy} = 0.5\%$
(a)
(b)
$\bar{\varepsilon}_{yy} = 0.5\%$
$\bar{\varepsilon}_{yy} = 0.5\%$
(c)
(d)

Fig. 13. Representation and Voronoi cell mesh for partially damaged RMEs at: (a) $\rho = 0$; (b) $\rho = 0.25$; (c) $\rho = 0.33$; (d) $\rho = 1$.

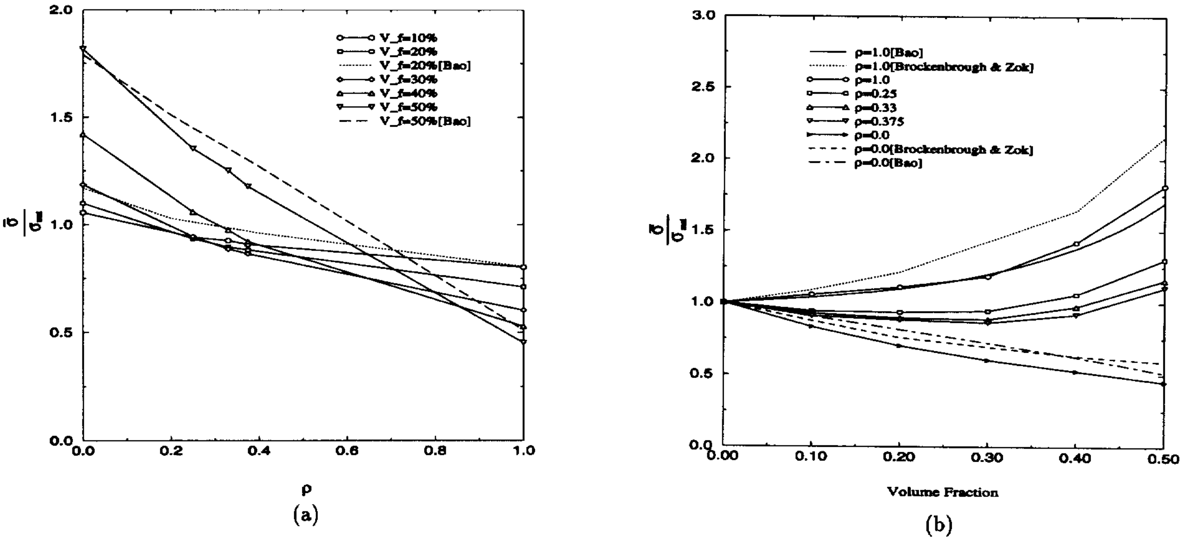

Fig. 14. Macroscopic stress response of partially damaged RMEs as a function of: (a) damage parameter ρ; (b) volume fraction.

$\nu = 0.33$; Post yield behavior (Ramberg–Osgood law) $\epsilon^p_m/\epsilon_0 = \alpha(\sigma_m/\sigma_0)^n$, with $\sigma_0 = 43$ MPa, $n = 10$, and $\alpha = 3/7$. The inclusions are brittle with Young's modulus $E = 350$ GPa, Poisson's ratio $\nu = 0.2$.

In [10], the matrix material is assumed to be rigid–plastic,while Brockenbrough and Zok [35] employs the Ramberg–Osgood law in their analysis. For undamaged Voronoi elements, the stress field in the matrix is represented by a 34 term expansion generated using 25 polynomial terms (6th order complete polynomial expansion, i.e. $p + q = 2 \cdots 6$) and 9 reciprocal terms (3 reciprocal terms for each polynomial exponent of 2, i.e. $i = p + q \cdots p + q + 2 \ \forall \ p + q = 2$), while the stress field in the inclusions are modeled using only 25 polynomial terms. Fewer reciprocal terms are used than in the previous example due to the smooth interface for circular inclusions. For cracked elements though, the additional reciprocal terms are the same as those in the previous example, i.e. $(i = p + q \cdots p + q + 2 \ \forall \ p + q = 2 \cdots 4)$.

The macroscopic stress as a function of the damage parameter ρ for various volume fractions are plotted in Fig. 14(a) at a macroscopic strain level of $\bar{\epsilon}_{yy} = 10\epsilon_0$. The ordinate $\bar{\sigma}/\sigma_m$ represents the ratio of the macroscopic stress to that in the pure matrix material at identical macroscopic strain levels. This is a measure of the strengthening or weakening due to the presence of partially damaged stiffer inclusions. The results indicate a near linear variation of the stress with ρ at all volume fractions, as concluded in [10] and [35]. Weakening of the fully damaged RMEs ($\rho = 1$) is more drastic with increase in the inclusion volume fraction, since less matrix material is available to carry the applied strain. Plots of the macroscopic stress as a function of the inclusion volume fractions, at various damage levels is depicted in Fig. 14(b). Except for the fully damaged case ($\rho = 1.0$), the surrounding undamaged inclusions lead to a stiffer response of the composite with increasing volume fraction, compared to the matrix material ($V_f = 0\%$). However, when all particles are damaged, i.e. $\rho = 1.0$, the stress capacity of the material element reduces significantly with increasing volume fraction. Good qualitative agreement is obtained with [10,35] for $\rho = 0, 1$, even though their analysis use axisymmetric unit cells.

4. Evolving damage in simulation of real micrographs

All examples in the previous sections consider pre-existing damage, and therefore do not involve crack initiation and change of element topology with increased loading. Also, the microstructures are computer simulated, and rather simple. The present example deals with continuously evolving microstructural topology through the onset and evolution of particle cracking in real microstructures. They correspond to micrographs obtained from detailed serial sectioning of reinforced Al–Si–Mg alloys developed by ALCOA [18] containing ~10% or 20% by weight of Si particulates. The material was prepared by a gas atomization process to precipitate equiaxed Si particles, followed by cold isostatic pressing [18]. Resulting billets were then canned, degassed at 450°C and consolidated to full density by hot isostatic pressing. Scanned micrographs of the sections are then digitized, and equivalent microstructures with elliptical inclusions are constructed by equating the 0th, 1st and 2nd moments of the equivalent ellipses with those of the actual inclusions Ω_c^e (see [25] for details). The procedure yields: (i) (x_c, y_c) the centroid of the ellipse, (ii) (a, b) the lengths of the major and minor axes, and (iii) θ the angular orientation of the major axis. A real optical micrograph of a section, the simulated equivalent microstructure and the Voronoi cell mesh obtained by tessellation are presented in Figs. 15(a, b and d), respectively. The equivalent microstructure consists of 97 Si inclusions for which the volume fraction is calculated to be $V_f = 18.6\%$. The microstructural representative material element modeled, has dimensions of

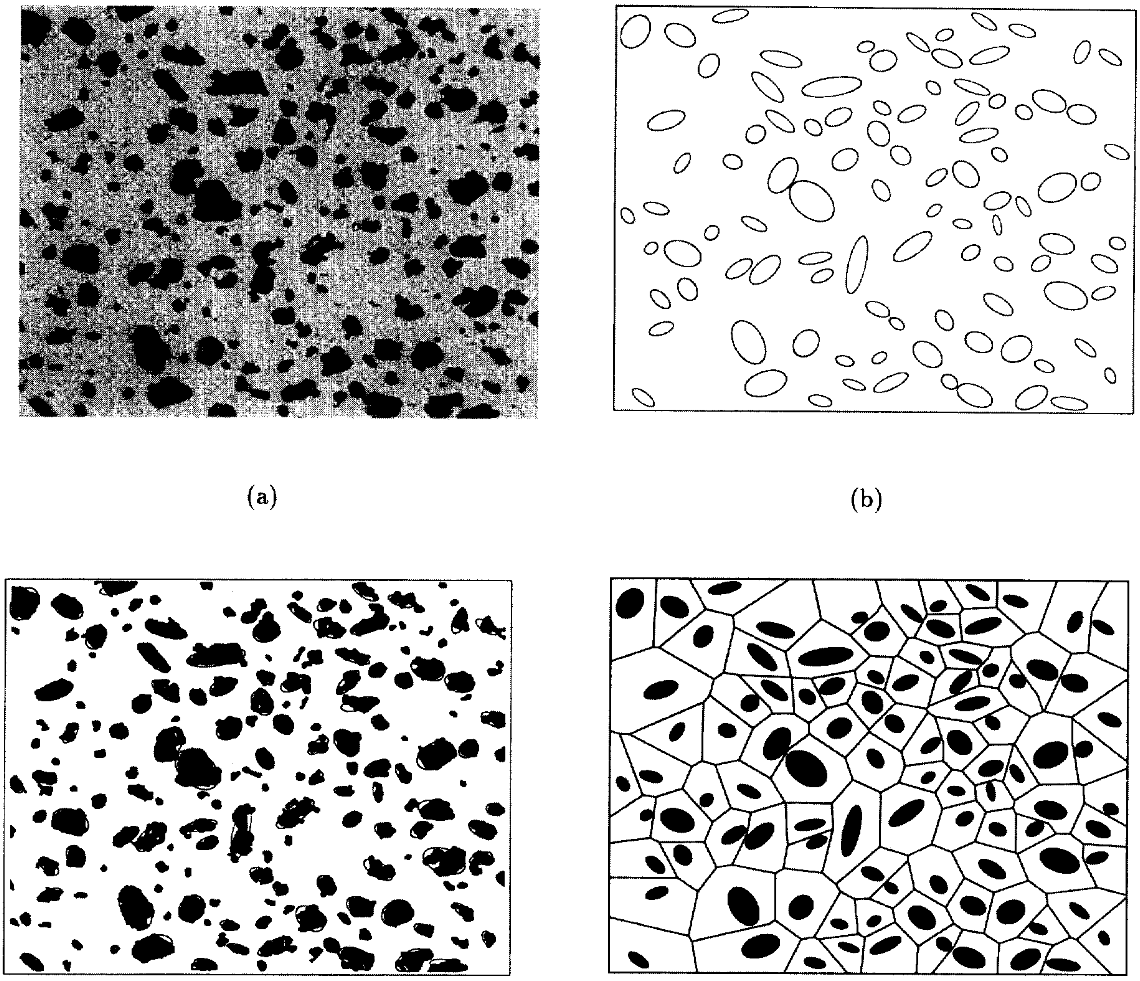
(a) (b)

(c) (d)

Fig. 15. (a) Optical micrograph of a section of Al–Mg–Si composite (20% Si); (b) simulated equivalent microstructure; (c) simulated microstructure superimposed on the micrograph; (d) Voronoi cell mesh resulting from tessellation.

$205\mu \times 180\mu$. The particles are of various sizes and shapes, and a histogram of equivalent size D distribution is presented in Fig. 16a. Though both 10% ($V_f = 9.1\%$) and 20% ($V_f = 18.6\%$) by weight composites are simulated in this study, the results shown are predominantly for the 20% composite.

The material properties of the ductile Al–Si–Mg Matrix are obtained from the stress–strain data presented in [19]. The Young's modulus is $E = 69$ GPa, and the Poisson's ratio is $\nu = 0.33$, while the post yield non-linear isotropic hardening behavior is obtained in a digitized form from the experimental data of Kiser et al. [19], as shown in Fig. 17. The properties of the brittle Si inclusions are assumed as, Young's modulus $E = 161$ GPa,

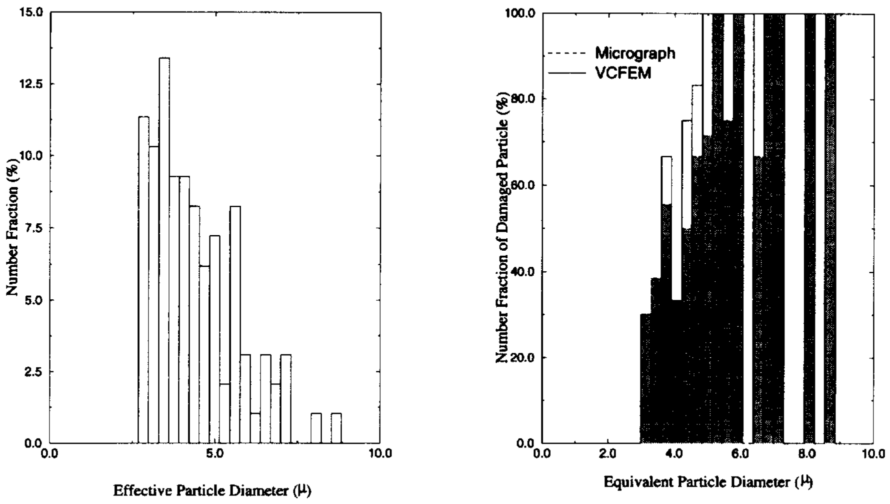

(a) (b)

Fig. 16. Particle size distribution from simulated microstructure of 20% Si Al–Mg–Si composite; (b) number fraction of damaged particles at $\bar{\epsilon}_{yy} = 6\%$ for 20% Al–Si–Mg composite. Ordinate is the fraction of particles cracked with respect to the total number of particles within the size range. Shaded regions are for micrographs and white regions are for simulation results.

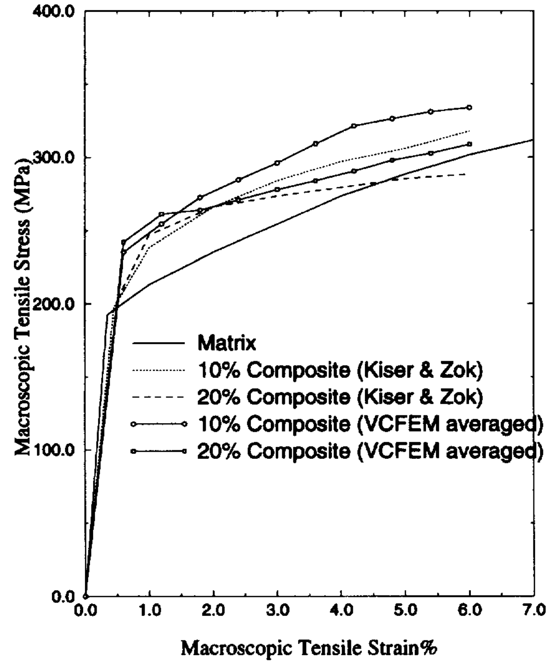

Fig. 17. Comparison of macroscopic stress–strain response with experimental results for real micrographs of Al–Si–Mg composite.

Poisson's ratio $\nu = 0.2$. The critical stress to particle crack initiation σ_{cr} is assumed to be also dependent on the particle dimensions as discussed in Eq. (29). The initial flaw size c in Eq. (29) is proportional to the average effective diameter of D_{avg} which is found to be 4.4μ. Certainly, the proportional dependence of the flaw size on D is an approximation that is admitted in this study for the sake of simplicity. In reality, the flaw may be distributed in a more complex manner, and this would require detailed experimental observations. The proportionality constant e is calculated based on a calibration study performed on auxiliary RMEs, which are modeled from micrographs of sections of different specimens. The estimate is obtained to be $e = c/D = 0.125$ or 12.5%, by comparison with the number of particles cracked in actual microstructure at the same overall strain level, and similar macroscopic behavior. Thus, the critical stress to fracture for individual particles is taken to be

$$\sigma_{\text{cr}} = \frac{K_{IC}}{\sqrt{c\pi}} = \frac{K_{IC}}{\sqrt{0.125D\pi}}$$

where $D = 4.4\mu$ and the fracture toughness for Si is obtained from a handbook as $K_{IC} = 0.6\,\text{MPa}\sqrt{m}$.

As in previous examples, the matrix material of the undamaged Voronoi elements are modeled using 34 stress coefficients (25 polynomial + 9 inclusion based reciprocal terms) and damaged elements are modeled using 70 stress coefficients (25 polynomial + 9 inclusion based reciprocal terms + 35 crack based reciprocal terms). The corresponding undamaged inclusions are modeled using 25 stress coefficients (25 polynomial terms), and the damaged inclusions are modeled using 61 stress coefficients (25 polynomial + 36 crack based reciprocal terms). The RMEs are analyzed with monotonic horizontal loading to a macroscopic strain of $\bar{\epsilon}_{xx} = 6\%$ under plain strain conditions. Complete particle splitting is considered in these simulations.

The overall macroscopic stress-strain response of the Al–Si–Mg composite for both the 10% and 20% compositions are compared with experimental results of Kiser and Zok [19], shown in Fig. 17. The VCFEM plots correspond to the average response of two sections of the same specimen. Despite the fact that VCFEM analysis is a two-dimensional approximation for three-dimensional materials, the comparison is very reasonable. The load-carrying capacity is in general higher for VCFEM predictions at all loading stages, which may be attributed to the constrained plastic flow arising out of plane strain constraints. Evolving microstructures, with continuous damage initiation at increasing load levels, are shown in Figs. 18 and 19 for the 10% and 20% composites, respectively. For the 20% composite, initial stages of particle cracking is noticed at $\bar{\epsilon}_{yy} = 1.2\%$. With continued macroscopic straining the larger particles fracture, and maximum number fraction of additional split particles are observed at $\bar{\epsilon}_{yy} = 3.0\%$. Additional loading causes much less additional damage. This behavior is also reflected in the macroscopic response, which exhibit less stiffness in earlier phases of plastic deformation. A comparison of damage levels for the simulation and observations in the actual micrograph at $\bar{\epsilon}_{xx} = 6\%$, is shown in Fig. 16(b). The ordinate represents the ration of the number of cracked particles in a size range to the total number of particles in that range. The white areas correspond to the simulated damage and the shaded regions represent damage levels in the micrograph. It can be seen that VCFEM predictions are identical to those in the micrograph for larger particle size. For smaller particle sizes, the analysis tends to overestimate the level of damage.

The distribution of principal stresses in the inclusions and the matrix plastic strains, at two stages of loading are shown, respectively, in Figs. 20 and 21.. Though the damaged particles contain sites of highly concentrated

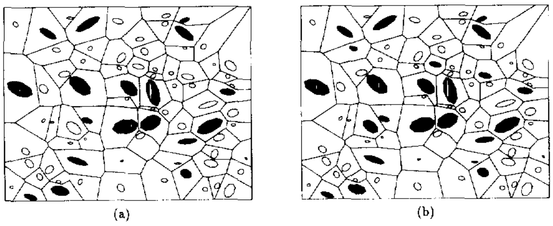
(a) (b)

Fig. 18. Deformed VCFEM meshes for simulated 10% Al–Si–Mg composite at: (a) $\bar{\epsilon}_{xx} = 4.2\%$; (b) $\bar{\epsilon}_{xx} = 6.0\%$. Cracked paritcled are blackened for clarity.

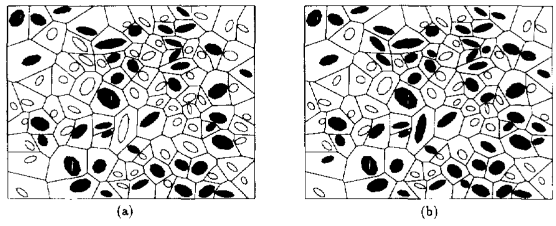
(a) (b)

Fig. 19. Deformed VCFEM meshes for simulated 20% Al–Si–Mg composite at: (a) $\bar{\epsilon}_{xx} = 4.2\%$; (b) $\bar{\epsilon}_{xx} = 6.0\%$. Cracked particles are blackened for clarity.

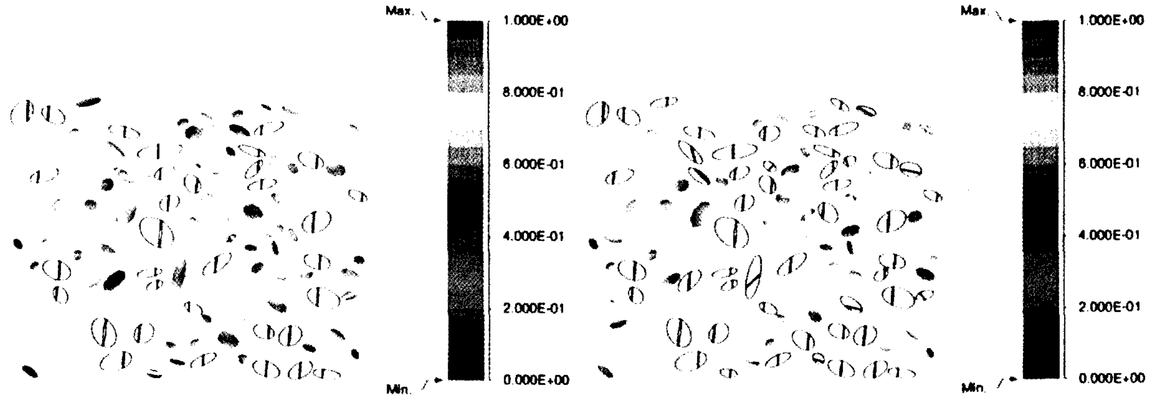

(a) (b)

Fig. 20. Principal stress distribution in uncracked particles at: (a) $\bar{\epsilon}_{xx} = 4.2\%$; (b) $\bar{\epsilon}_{xx} = 6.0\%$ for microstructure with 20% Si. Principal stress values are scaled to critical stresses σ_{cr} of respective particles. Principal stresses in the matrix and cracked particles are not shown.

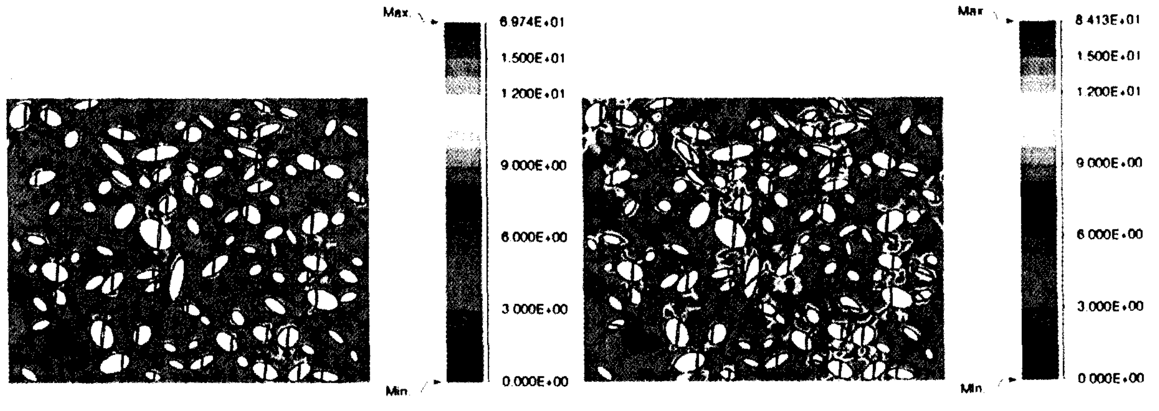

(a) (b)

Fig. 21. Equivalent plastic strain (%) in the for simulated microstructure with 20% Si at: (a) $\bar{\epsilon}_{xx} = 4.2\%$; and (b) $\bar{\epsilon}_{xx} = 6.0\%$.

stresses, the principal stress distribution is only shown for undamaged particles to depict future sites of damage in the microstructure. These stresses are scaled with respect to σ_{cr} of that particle, such that a value greater than 1 signals a potential damage site. It is interesting to note that even though some large particles achieve high stress levels early on in the loading, they remain intact for the entire loading path without cracking. Damage of other particles in their neighborhood, causes a stress re-distribution and shielding for some particles at the threshold of failure. The matrix plastic strain distribution in Fig. 21(a) shows regions of localized plastic flow near the crack tips of damaged particles. A particle crack induces large plastic flow in the neighboring matrix which causes the stress to rise in particles in this region and eventually initiate a crack. The plastic deformation flows in the form of a band from one cracked particle to the next. The remainder of the matrix undergoes relatively smaller deformations. From the localization bands in Fig. 21(b), it is expected that catastrophic failure in the microstructure would result had the matrix been allowed to soften.

5. Conclusions

In this paper, the Voronoi Cell Finite Element Method (VCFEM) is developed for stress analysis in heterogeneous ductile matrix microstructures with evolving damage in the form of particle cracking. VCFEM is a material morphology based finite element model, in which the mesh is generated by Dirichlet tessellation of the microstructure. The uniqueness of the present method lies in its ability to model continuously changing element topology through the initiation of the crack phase as a function of changing loads. The computational scheme allows for automatic regeneration of new topologies introduced by progressive failure, and avoids any user interference for rediscretizing the evolving microstructure.

Verification of the VCFEM for microstructural damage is established by a wide variety of comparison studies. These include comparison with analytical results, other numerical studies in literature and simulations done with conventional finite element packages. These studies are predominantly for simple morphologies, and mostly with pre-existing cracks. Very good agreement is obtained in most of these comparison studies, both from a macroscopic and microscopic point of view. The main advantage of this method is that it can be used for analyzing damage in real micrographs, which is rather difficult with most computational and analytical schemes. Generally good concurrence of VCFEM produced macroscopic stress-strain results is obtained with experimental response on Al–Si–Mg composite systems at different volume fractions. Microscopic information from experiments is only available in the form of damaged particles at certain overall strain levels for the specimens recorded. Reasonably good agreement with VCFEM predictions is even obtained in this respect, where the extent of particle fracture for different size ranges is compared. The efficiency of the VCFEM codes is also noteworthy. A direct comparison with conventional FEM packages for undamaged random materials show a ~30–50 times reduction in computing time. Coupled with significantly reduced modeling efforts, VCFEM has tremendous prospects as an advanced material modeling tool.

Acknowledgments

The authors would like to thank Dr. O. Richmond, Dr. W.H. Hunt and Dr. T.R. Rouns of ALCOA Technical Center for their help on the experimental portion of this work. This work has been sponsored by the United States Army Research Office through Grant No. DAAHO4-95-1-0176 (Program Director: Dr. K.R. Iyer) and by the Mechanics and Materials program (Program Director O. Dillon) of the National Science Foundation through Grant No. MSS-9301807, and by a grant from the ALCOA Technical Center. Computer support was provided by the Ohio Supercomputer Center through grant #PAS813-2.

References

[1] J. Lemaitre, A Course on Damage Mechanics (Springer Verlag, 1992).

[2] T.E. Lacy, D.L. McDowell and P.A. Willice, Effects of damage distribution on evolution, ASTM, in review.

[3] T.E. Lacy, D.L. McDowell, P.A. Willice and R. Talreja, On representation of damage evolution in continuum damage mechanics, Acta. Metall. Mater., in review.

[4] Z. Hashin, The differential scheme and its applications to cracked materials, J. Mech. Phys. Solids 36 (1988) 719–734.

[5] Y.-Z. Chen, General case of multiple crack problems in an infinite plate, Engrg. Fract. Mech. 38 (1984) 379–404.

[6] A. Chudnovsky, A. Dolgopolsky and M. Kachanov, Elastic solution of a crack with a microcrack array: Parts I and II, Int. J. Solids Struct. 23 (1987) 1–21.

[7] C.F. Shih and R.J. Asaro, Elastic-plastic analysis of cracks on bimaterial interfaces. Part II. Structure of small scale yielding fields, J. Appl. Mech. 56 (1989) 763–779.

[8] A.G. Evans, B.J. Dagleish, M.Y. He and J.W. Hutchinson, On crack path selection and the interface fracture energy in bimaterial systems, Acta Metall. Mater. 37 (1989) 3249–3254.

[9] V. Tvergaard, Model studies of fibre breakage and debonding in a metal reinforced by short fibers, J. Mech. Phys. Solids 41 (1991) 1309–1326.

[10] G. Bao, Damage due to fracture of brittle reinforcements in a ductile matrix, Acta Metall. Mater. 40 (1992) 2547–2555.

[11] C.L. Hom, P.A. Mataga and R.M. McMeeking, Some recent developments in numerical modelling of fracture toughness in brittle matrix composites, Int. J. Numer. Methods Engrg. 27 (1989) 233–255.

[12] Y. Sugimura, P.G. Lim, C.F. Shih and S. Suresh, Fracture normal to a bimaterial interface: Effects of plasticity on crack-tip shielding and amplification, Acta Metall. Mater. 43 (1995) 1157–1169.

[13] M. Finot, Y.-L. Shen, A. Needleman and S. Suresh, Micromechanical modeling of reinforcement fracture in particle reinforced-matrix composites, Metall. Mat. Trans. A 25A (1994) 2403–2420.

[14] J.R. Brockenbrough, S. Suresh and W.A. Weinecke, Deformation of metal-matrix composites with continuous fibers: Geometrical effects of fiber distribution and shape, Acta Metall. Mater. 39 (1991) 735–752.

[15] T. Christman, A. Needleman and S. Suresh, An experimental and numerical study of deformation in metal-ceramic composites, Acta Metall. Mater. 37 (1989) 3029–3050.

[16] P.E. McHugh, R.J. Asaro and C.F. Shih, Computational modeling of metal-matrix composite materials, Parts I–IV, Acta Metall. Mater. 41 (1993) 1461–1510.

[17] W.H. Hunt, J.R. Brockenbrough and P.E. Magnusen, An Al–Si–Mg composite model system: Microstructural effects on deformation and damage evolution, Scripta Metall. Mater. 25 (1991) 15–20.

[18] W.H. Hunt, Microstructural damage processes in an aluminum matrix-silicon particle composite model, Ph.D. Thesis, Carnegie Mellon University, 1992.

[19] M.T. Kiser, F.W. Zok and D.S. Wilkinson, Plastic flow and fracture of a particulate metal matrix composite, Acta Metall. Mater. 9 (1996) 3465–3476.

[20] S. Moorthy and S. Ghosh, A model for analysis of arbitrary composite and porous microstructures with Voronoi cell finite elements, Int. J. Numer. Methods Engrg. 39 (1996) 2363–2398.

[21] S. Ghosh and S. Moorthy, Elastic-plastic analysis of arbitrary heterogeneous materials with the Voronoi cell finite element method, Comput. Methods Appl. Mech. Engrg. 121 (1995) 373–409.

[22] S. Moorthy, S. Ghosh and Y. Liu, Voronoi cell finite element method for micropolar thermo-elastic, elasto-plastic heterogeneous materials, ASME Appl. Mech. Rev. 47 (1993) 207–221.

[23] R.V. Churchill and J.W. Brown, Complex Variables and Application (McGraw-Hill, 1990).

[24] N.I. Muskhelishvili, Some Basic Problems in the Mathematical Theory of Elasticity (P. Nordhoff Ltd., 1961).

[25] S. Moorthy, The Voronoi cell finite element method for response and damage analysis of arbitrary heterogeneous media, Ph.D. Thesis, Ohio-State University, 1997.

[26] R. Hill, The mathematical Theory of Plasticity (Oxford University Press, 1950).

[27] W.A. Curtin, In situ fiber strengths in ceramic-matric composites from fracture mirrors, J. Am. Cer. Soc. 77 (1994) 1075–1078.

[28] T. Amornsakchai, The relation between filament diameter and fracture strength for ultra-high-modulus polyethelene fibers, J. Mat. Sci. 28 (1993) 1689–1698.

[29] H. Matthies and G. Strang, The solution of nonlinear finite element equations, Int. J. Numer. Methods Engrg. 14 (1979) 1613–1626.

[30] J.W. Hutchinson, Singular behavior at the end of a tensile crack in a hardening material, J. Mech. Phys. Solids 16 (1968) 13–31.

[31] J.L. Sanders, On the Griffith–Irwin fracture theory, J. Appl. Mech. 27 (1960) 352–353.

[32] J.R. Rice and G.F. Rosengren, Plane strain deformation near a crack tip in a power-law hardening material, J. Mech. Phys. Solids 16 (1968) 1–12.

[33] R.M. McMeeking, Finite deformation analysis of crack-tip opening in elastic-plastic materials and implications for fracture, J. Mech. Phys. Solids 25 (1977) 357–381.

[34] Hibbit, Karlsson & Sorenson, Inc., Abaqus Users Manual, 1994.

[35] J.R. Brockenbrough and F.W. Zok, On the role of particle cracking in flow and fracture of metal matrix composites, Acta Metall. Mater. 40 (1993) 2547–2555.